

## Evidence for Centrifugal Breakout around the Young M Dwarf TIC 234284556

ELSA K. PALUMBO,<sup>1</sup> BENJAMIN T. MONTET,<sup>2</sup> ADINA D. FEINSTEIN,<sup>3,\*</sup> LUKE G. BOUMA,<sup>4</sup> JOEL D. HARTMAN,<sup>4</sup> LYNNE A. HILLENBRAND,<sup>1</sup> MICHAEL A. GULLY-SANTIAGO,<sup>5</sup> AND KIRSTEN A. BANKS<sup>2</sup>

<sup>1</sup>Department of Astronomy, California Institute of Technology, 1216 E California Blvd, Pasadena, CA 91125, USA

<sup>2</sup>School of Physics, University of New South Wales, Sydney, NSW 2052, Australia

<sup>3</sup>Department of Astronomy and Astrophysics, University of Chicago, 5640 S. Ellis Ave, Chicago, IL 60637, USA

<sup>4</sup>Department of Astrophysical Sciences, Princeton University, 4 Ivy Lane, Princeton University, Princeton, NJ 08544, USA

<sup>5</sup>Department of Astronomy, University of Texas at Austin, 2515 Speedway, Stop C1400, Austin, Texas 78712-1205, USA

### ABSTRACT

Magnetospheric clouds have been proposed as explanations for depth-varying dips in the phased light curves of young, magnetically active stars such as  $\sigma$  Ori E and RIK-210. However, the stellar theory that first predicted magnetospheric clouds also anticipated an associated mass-loss mechanism known as centrifugal breakout for which there has been limited empirical evidence. In this paper, we present data from *TESS*, LCO, ASAS-SN, and Veloce on the 45 Myr M3.5 star TIC 234284556, and propose that it is a candidate for the direct detection of centrifugal breakout. In assessing this hypothesis, we examine the sudden ( $\sim$ 1-day timescale) disappearance of a previously stable ( $\sim$ 1-month timescale) transit-like event. We also interpret the presence of an anomalous brightening event that precedes the disappearance of the signal, analyze rotational amplitudes and optical flaring as a proxy for magnetic activity, and estimate the mass of gas and dust present immediately prior to the potential breakout event. After demonstrating that our spectral and photometric data support a magnetospheric clouds and centrifugal breakout model and disfavor alternate scenarios, we discuss the possibility of a coronal mass ejection (CME) or stellar wind origin of the corotating material and we introduce a reionization mechanism as a potential explanation for more gradual variations in eclipse parameters. Finally, after comparing TIC 234284556 with previously identified “flux-dip” stars, we argue that TIC 234284556 may be an archetypal representative of a whole class of young, magnetically active stars.

*Keywords:* M dwarf stars, stellar magnetic fields, stellar coronal mass ejections, stellar flares, stellar winds

### 1. INTRODUCTION

Young ( $\lesssim$ 100 Myr) stars have important implications for planet formation, evolution, and habitability because they tend to be magnetically active (e.g. Feigelson et al. 1991; Vidotto et al. 2014), their planets tend to be rapidly evolving (Mann et al. 2020), and their protoplanetary disks may not yet have dissipated (e.g. Williams & Cieza 2011). In particular, they can teach us about how, when, and why atmospheric evolution, planetary migration, and other dynamical interactions take place (e.g. Rizzuto et al. 2020). For example, some pre-main sequence stars have X-ray flares that, at their peak lumi-

nosity, release more energy in one second than the total X-ray energy from any known solar flare (Getman & Feigelson 2021). The ionizing radiation from such flares impacts accretion, disk chemistry, and atmospheric erosion (Benz & Güdel 2010; Waggoner & Cleeves 2019). Coronal mass ejections (CMEs)—mass-loss events potentially connected to such flaring activity—may influence radionuclide production in protoplanetary disks, planetary dynamos, and the clearing of debris disks (Osten & Wolk 2015).

Young stars exhibit many different classes of photometric variability. One type is the quasi-periodic dimming events of the “dipper” stars, likely caused by non-uniformly distributed gas and dust in the protoplanetary disk (Bodman et al. 2017; Cody & Hillenbrand 2010; Ansdel et al. 2016). Dippers are very common, accounting for 20–30% of young stellar objects (McGinnis et al.

Corresponding author: Elsa K. Palumbo  
 epalumbo@caltech.edu

\* NSF Graduate Research Fellow

2015; Ansdel et al. 2019). Their deep (up to 50%), often aperiodic eclipse events (Stauffer et al. 2015; Cody & Hillenbrand 2018) and strong infrared excesses (Hedges et al. 2018) make them easily detectable in time-series photometry and therefore useful for studying disk evolution and planet formation.

More recently, stars without significant infrared excesses but rapid, periodic photometric variability have been identified. Stauffer et al. (2017, 2018, 2021) describe three families of young M dwarfs that exhibit periodic photometric variability that appears to be synchronous with stellar rotation but that does not fit cleanly into previously established categories:

1. Scallop shell stars—rapidly-rotating ( $P_{\text{rot}} < 0.65$  days) M dwarfs whose light curves exhibit multiple wavelike dips that are typically stable over  $\sim 75$ - to 80-day timescales. Such dips have been seen to undergo sudden morphological changes (Stauffer et al. 2017).
2. Persistent flux-dip stars—stars with discrete triangularly shaped dips in their light curves. Similarly to scallop shells, dimming events have been seen to suddenly change in depth (Stauffer et al. 2017).
3. Transient flux-dip stars—stars with a single prominent and roughly triangular dip. The depth of the dip may vary significantly from period to period, with more gradual changes sometimes occurring over longer timescales (Stauffer et al. 2017). RIKE-210 is one particularly well-characterized example of such an object (David et al. 2017).

Work by Günther et al. (2020) has since shown that the distinction between scallop shells and flux-dip stars may be due only to an observational bias and their quick rotation periods. These authors suggest that a low-cadence sampling rate leads to smearing which makes flux-dip stars look like scallop shells.

One well-known example of a flux-dip star is the 7-10 Myr old PTFO 8-8695, which exhibits 0.45-day-period transit-like dips with shapes, depths, and duration that have varied over a decade of observation and that are synchronous with the host star's rotation (van Eyken et al. 2012; Yu et al. 2015). The proposed explanations for the dips for this system have ranged from a precessing Jovian planet (Barnes et al. 2013) to an accretion hotspot (Yu et al. 2015), or even a small dusty planet (Tanimoto et al. 2020). More recently, Bouma et al. (2020a) have suggested circumstellar material as a likely explanation based on a synthesis of earlier ground-based observations with data from the Transiting Exoplanet Survey Satellite (*TESS*; Ricker et al. 2014).

Partly because of their strong magnetic fields and rapid rotation, the light curves of young stars have also been searched for clues of star-planet and star-disk interactions (e.g. Johnstone et al. 2013), and have been used to test magnetism-related stellar theory. One notable example is  $\sigma$  Ori E, a  $\approx 1.1$  Myr, B2 star in the Orion complex (Townsend et al. 2013). This star's light curve features distinctive double dips with periodicity matching that of the star's rotational period (e.g. Townsend et al. 2013). Although these dips are morphologically similar to the eclipses of an eclipsing binary (Townsend 2007), radial velocity data has shown them to be inconsistent with their being caused by a massive ( $> 0.04M_{\odot}/\sin i$ ) companion (Groote & Hunger 1977).

This mystery led to a search for alternative explanations for  $\sigma$  Ori E's dips, one centered around magnetic interactions. In particular, Townsend (2007) demonstrated that a Rigidly Rotating Magnetosphere (RRM; Townsend & Owocki 2005) model could recreate  $\sigma$  Ori E's photometric and spectroscopic variability. Under this model,  $\sigma$  Ori E's dips would be caused by two co-rotating circumstellar plasma clouds originating from stellar winds (Townsend 2007). Because of  $\sigma$  Ori E's strong magnetic field and rapid rotation, the stellar wind would accumulate into relatively dense, stable regions within the star's magnetic field (Owocki & Cranmer 2017). Several shortcomings of the RRM model have since been highlighted (Oksala et al. 2015), however the theory of magnetospheric clouds is widely accepted for the origin of  $\sigma$  Ori E's variability (Townsend 2007; Oksala et al. 2010; Townsend et al. 2013).

Importantly,  $\sigma$  Ori E is one of only a handful of stars in the literature for which magnetospheric clouds have been proposed as a dip-causing mechanism. The other candidates are all much lower mass stars, including the M2.5 star RIKE-210 (David et al. 2017) and other candidates discussed by Stauffer et al. (2017, 2018, 2021); Zhan et al. (2019). Considering the brightness of  $\sigma$  Ori E ( $V = 6.46 \pm 0.01$ ; Hernández et al. 2014), it may not be surprising that it has become a test case for the existing theories of stellar magnetism. In particular, since there is a critical point beyond which the magnetic force can no longer contain the magnetospheric cloud's material by balancing the centrifugal force, theory demands some sort of a mass-loss mechanism (e.g. Owocki & Cranmer 2017; Shultz et al. 2020).

One such proposed mass-loss mechanism is centrifugal breakout, in which the ionized gas and dust that makes up the magnetospheric clouds accumulates, dragging the magnetic field lines along with it, until the cloud becomes so massive that the magnetic loops constraining the corotating material are stressed andulti-

mately broken. This centrifugal breakout event would coincide with the previously trapped material being suddenly expelled, with the magnetic field lines reconnecting immediately afterwards. (e.g. Townsend & Owocki 2005). This mechanism has a number of advantages: (1) it can be derived from first principles (see Townsend & Owocki 2005), (2) it is consistent with 2-D magnetohydrodynamic simulations (ud-Doula et al. 2006), and (3) it is supported by stars' observed H  $\alpha$  emission (Shultz et al. 2020). However, Townsend et al. (2013) did not detect any evidence of breakout around  $\sigma$  Ori E, leading to a consideration of alternate mechanisms, such as the diffusion-plus-drift model of Owocki & Cranmer (2017).

Here, we consider the light curve of TIC<sup>1</sup> 234284556<sup>2</sup>, a  $\approx$  45-million-year-old,  $0.42 \pm 0.02 M_{\odot}$  star in the Tucana-Horologium association (Kraus et al. 2014) which has co-rotating dip-like features that resemble those of PTFO 8-8695,  $\sigma$  Ori E, and others (e.g. Stauffer et al. 2017, 2018, 2021; Zhan et al. 2019). Notably, we observe a 1.2%-deep dip that had been present in data from the previous 24 days disappear within a  $\sim$ 1-day interval. We interpret this as evidence for a potential centrifugal breakout event, with more gradual changes in eclipse parameters hinting at a separate role for an additional mass-loss mechanism.

TIC 234284556 stands out because it is relatively bright, with  $I = 11.68$  (Denis 2005), and nearby, at  $44.102 \pm 0.028$  pc (Bailer-Jones et al. 2021), compared to  $\approx$ 130 pc for the younger transient flux-dip stars in the Taurus, Upper Sco, and UCL/LCC clusters. This star has been observed by the *TESS* mission for  $\sim$  three months over two years. Besides being a promising target for follow-up observations, TIC 234284556's low mass ( $0.422 M_{\odot}$ ) also hints at alternatives to  $\sigma$  Ori E's stellar wind mechanism for mass accumulation, such as CMEs.

This paper is organized as follows: In Section 2, we present our photometric and spectroscopic observations of TIC 234284556, which include data from *TESS*, the All-Sky Automated Survey for Supernovae (ASAS-SN), the Veloce-Rosso spectrograph, and the Las Cumbres Observatory (LCO). In Section 3, we present our analysis of this data and examine depth variations, flare rates, and other relevant features of the light curves. In Sections 4 and 5, we discuss potential origins of the observed dips and compare our findings with the theoret-

ical predictions of centrifugal breakout. In Section 6, we introduce a mechanism that could be behind more gradual changes in dip size, discuss stellar wind and CME sources of the co-rotating material, and examine our system in the broader context of young stars with similar variability. Finally, Section 7 summarizes our findings, their implications, and the role of future work.

## 2. OBSERVATIONS

### 2.1. Stellar Parameters

TIC 234284556 is an M3.5 star and a bona fide member of the Tucana-Horologium association (Tuc-Hor), a young moving group with an age of 35-45 Myr (Bell et al. 2015; Crundall et al. 2019). Its membership has been previously confirmed based on its proper motion and spectroscopic signatures of youth (Kraus et al. 2014). Moreover, its short and high-amplitude rotational signal is qualitatively consistent with what would be expected from a young star (e.g. Reinhold & Gizon 2015).

Using data from 2MASS, WISE, SDSS, APASS, Gaia, and Galex (Table 1), we constructed the spectral energy distribution of our target (Figure 1), comparing to the NextGen model (Hauschildt et al. 1999) atmosphere library for stars of similar temperature and metallicity. We find the SED is well-described by a  $3100 \pm 60$  K model atmosphere with no infrared excess or interstellar extinction; this temperature is consistent with the estimate of  $3249 \pm 157$  K provided by (Stassun et al. 2019). The lack of IR excess indicates that the primordial protoplanetary disk has already dissipated, effectively ruling out a dip-causing mechanism due to a massive, extended disk, as observed in the dipper stars.

TIC 234284556 has a Renormalized Unit Weight Error (RUWE) of 1.348 (Gaia Collaboration 2020), which, in some contexts, might be considered suggestive of astrometric binarity (e.g. Belokurov et al. 2020). However, Figure 2's plot of the RUWE of the high-confidence Tuc-Hor members from Gagné et al. (2018) shows a color-dependence, with Tuc-Hor members of a similar color having on average similar RUWE values, casting doubt on the binary interpretation. For an independent confirmation of this assessment, we plotted the Hertzsprung-Russel diagram for the same list of high-confidence Tuc-Hor members (Figure 2), finding TIC 234284556 to be consistent with the expected position for a single star.

### 2.2. *TESS*

*TESS* (Ricker et al. 2014) observed TIC 234284556 in three sectors over two years: Sector 1 (2018 July 25 - 2018 August 22), Sector 27 (2020 July 4 - 2020 July 30), and Sector 28 (2020 July 30 - 2020 August 26). TIC 234284556 was pre-selected as a short cadence target

<sup>1</sup> *TESS* Input Catalog (TIC; Stassun et al. 2018)

<sup>2</sup> This star is also known as UCAC4 135-177645, 2MASS J22223966-6303258, WISE J222239.75-630326.5, DENIS J222239.6-630325, UPM J2222-6303, Gaia DR2 6405089921141776128, or APASS 31766662.

**Table 1.** Wavelength-Specific Magnitudes for TIC 234284556

Bandpass	Value	Reference
WISE4 [22.24 $\mu\text{m}$ ]	8.644 $\pm$ 0.345	Cutri et al. (2021)
WISE3 [11.56 $\mu\text{m}$ ]	8.867 $\pm$ 0.027	Cutri et al. (2021)
WISE2 [4.600 $\mu\text{m}$ ]	9.012 $\pm$ 0.020	Cutri et al. (2021)
WISE1 [3.350 $\mu\text{m}$ ]	9.192 $\pm$ 0.024	Cutri et al. (2021)
H [2.159 $\mu\text{m}$ ]	9.345 $\pm$ 0.023	Cutri et al. (2003)
K [1.662 $\mu\text{m}$ ]	9.588 $\pm$ 0.026	Cutri et al. (2003)
J [1.235 $\mu\text{m}$ ]	10.183 $\pm$ 0.024	Cutri et al. (2003)
RP [0.799 $\mu\text{m}$ ]	11.9727 $\pm$ 0.0037	Gaia Collaboration (2018)
i [0.759 $\mu\text{m}$ ]	12.489 $\pm$ 0.04	Zacharias et al. (2012)
G [0.673 $\mu\text{m}$ ]	13.2072 $\pm$ 0.0016	Gaia Collaboration (2018)
r [0.617 $\mu\text{m}$ ]	14.038 $\pm$ 0.00	Zacharias et al. (2012)
V [0.544 $\mu\text{m}$ ]	14.645 $\pm$ 0.02	Zacharias et al. (2012)
BP [0.532 $\mu\text{m}$ ]	14.8351 $\pm$ 0.0079	Gaia Collaboration (2018)
g [0.469 $\mu\text{m}$ ]	15.338 $\pm$ 0.01	Zacharias et al. (2012)
B [0.436 $\mu\text{m}$ ]	16.245 $\pm$ 0.08	Zacharias et al. (2012)

**Table 2.** Summary of Stellar Parameters for TIC 234284556

Parameter	Value	Reference
TESS Designation	TIC 234284556	Stassun et al. (2019)
Gaia DR2 Designation	6405089921141776128	
RA [J2000]	22h 22m 39.69s	Gaia Collaboration (2020)
Dec [J2000]	-63° 03' 25.83"	Gaia Collaboration (2020)
Spectral Type	M3.5	Kraus et al. (2014)
$m_{TESS}$	11.8868 $\pm$ 0.0080	Stassun et al. (2019)
$I_{mag}$	11.68 $\pm$ 0.03	Denis (2005)
$V \sin i$ [km $\text{s}^{-1}$ ]	11.9 $\pm$ 0.9	Kraus et al. (2014)
$P_{\text{rot}}$ [days]	1.1066 $\pm$ 0.0003	This Work
Distance [pc]	44.102 $\pm$ 0.028	Bailer-Jones et al. (2021)
Mass [ $M_{\odot}$ ]	0.422 $\pm$ 0.020	Stassun et al. (2019)
Radius [ $R_{\odot}$ ]	0.428 $\pm$ 0.013	Stassun et al. (2019)
$T_{\text{eff}}$ [K]	3100 $\pm$ 60	This work
Age [Myr]	45 $\pm$ 4	Bell et al. (2015)
$\log(g)$ [cm $\text{s}^{-2}$ ]	4.8014 $\pm$ 0.0051	Stassun et al. (2019)

through the TESS Guest Investigator program and is also available in the Full-Frame Images (FFIs).<sup>3</sup>

As a precaution against data processing effects, we compared results from both short-cadence and FFI light curves throughout this work, where we relied on the open-source Python package `eleanor` (Feinstein et al. 2019) for extracting light curves from the FFIs. However, for our final analysis, we used all of the data-quality flagged two-minute-cadence *TESS* data from

NASA Ames’ Science Processing and Operations Center (SPOC) pipeline (Jenkins et al. 2016). The resulting short-cadence *TESS* light curves are shown in 3, with phase folded and stacked versions of the same data in Figure 4.

In our original data processing, we applied Gaussian Process (GP) regression to the long-cadence data in order to model TIC 234284556’s rotational signal. More specifically, we used the `gp.terms.RotationTerm` kernel from the Python package `exoplanet` (Foreman-Mackey et al. 2017, 2020) to models stellar variability as the combined behavior of two underdamped simple harmonic

<sup>3</sup> The target was proposed in program GI G011175, G011266, G011180, G03265 and G03226

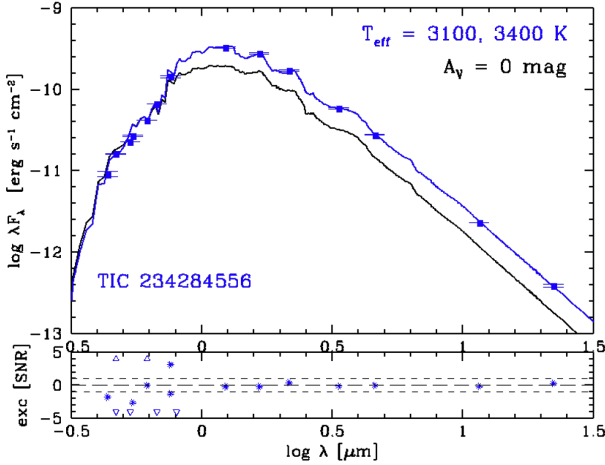


**Figure 1.** Spectral Energy Distribution (SED) for TIC 234284556 along with atmospheric models at the approximate  $\pm 1\sigma$  range of the Stassun et al. (2019) temperature estimate for this star. For low levels of extinction, this plot suggests an effective temperature near the lower limit presented in Stassun et al. (2019). Unlike the dipper stars, but like the stars (described by Stauffer et al. 2017, 2018; Zhan et al. 2019; Stauffer et al. 2021), TIC 234284556 lacks any detectable infrared excess, indicating that its dimming events are not caused an extended protoplanetary disk.

oscillators, one with a period corresponding to the rotational period of the star, and the other with half that period. We then used an iterative approach to define hyperparameters describing the GP, and to identify and mask outliers.

With this GP fit, stellar rotation was removed from the *TESS* short-cadence data; we detected a dip with an orbital period of  $1.1065 \pm 0.0037$  days and a depth of  $0.487 \pm 0.043\%$  over the sector. A closer investigation identified that the dip duration and depth varies gradually over the sector, ranging from 0.12% to 0.75% over the course of Sector 1. The dip’s period is consistent with the  $1.1071 \pm 0.0036$  day stellar rotation period that we measured from the GP, suggesting a co-rotating object. Moreover, the shape of the event appears to be asymmetric, with a slower egress than ingress.

This system was re-observed by *TESS* in Sectors 27 and 28. In Sector 27, a very similar dip is apparent, although with a deeper depth,  $0.756 \pm 0.043\%$  overall, with variation from 0.38% to 1.2% over the sector. We also see a change in phase and a reversal of the asymmetry, with the ingress now slower than the egress, a phenomenon discussed in more detail in Section 3.2. Surprisingly, in Sector 28 there is no detectable periodic dip, even though it is separated from Sector 27 by only 1.2 days.

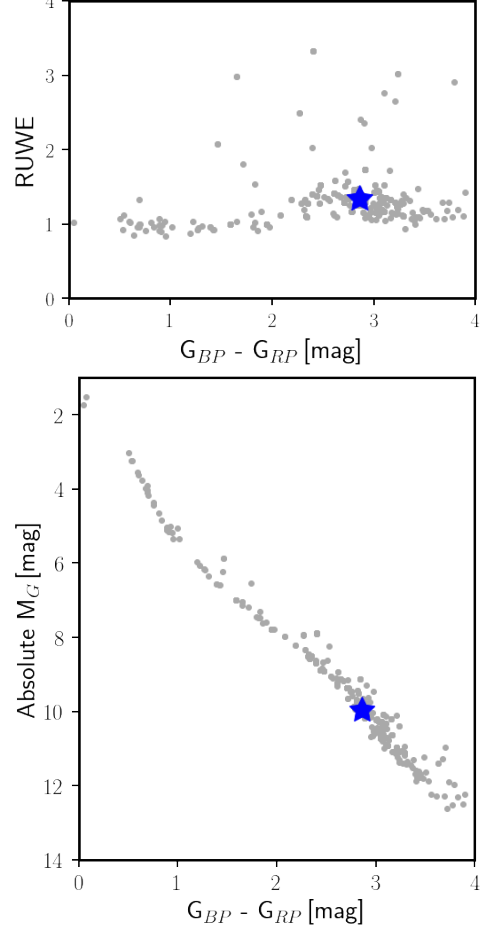


**Figure 2.** Evidence for nonbinarity of TIC 234284556. Point estimates for TIC 234284556 (blue star) and all other high confidence Tuc-Hor members (gray circles) are shown, where a difference of Gaia’s Rp and Bp bandpasses is used to quantify a star’s color, a proxy for spectral type. Top Panel: Assessing astrometric binarity. Note the color-dependence of typical RUWE values, which casts doubt on the interpretation that TIC 234284556’s RUWE of 1.348 is indicative of it being an astrometric binary. Bottom Panel: Assessing photometric binarity. Note that the point estimate for TIC 234284556 is not above the intrinsic scatter, suggesting that our target is not a photometric binary.

At a time that coincides with the rapid disappearance of the eclipse and immediately before the end of Sector 27, we see an anomalous brightening event with a morphology unlike the typical steep rise and exponential decay exhibited by a stellar flare (see the last partial orbit of Sector 27 in Figure 4). Although *TESS* data near the start and end of an orbit can have significant systematics, this signal does not appear to be related to scattered Earthshine. Instead, we see similar behavior across the entire pixel response function, and neighboring stars do not exhibit such a feature, so we infer that

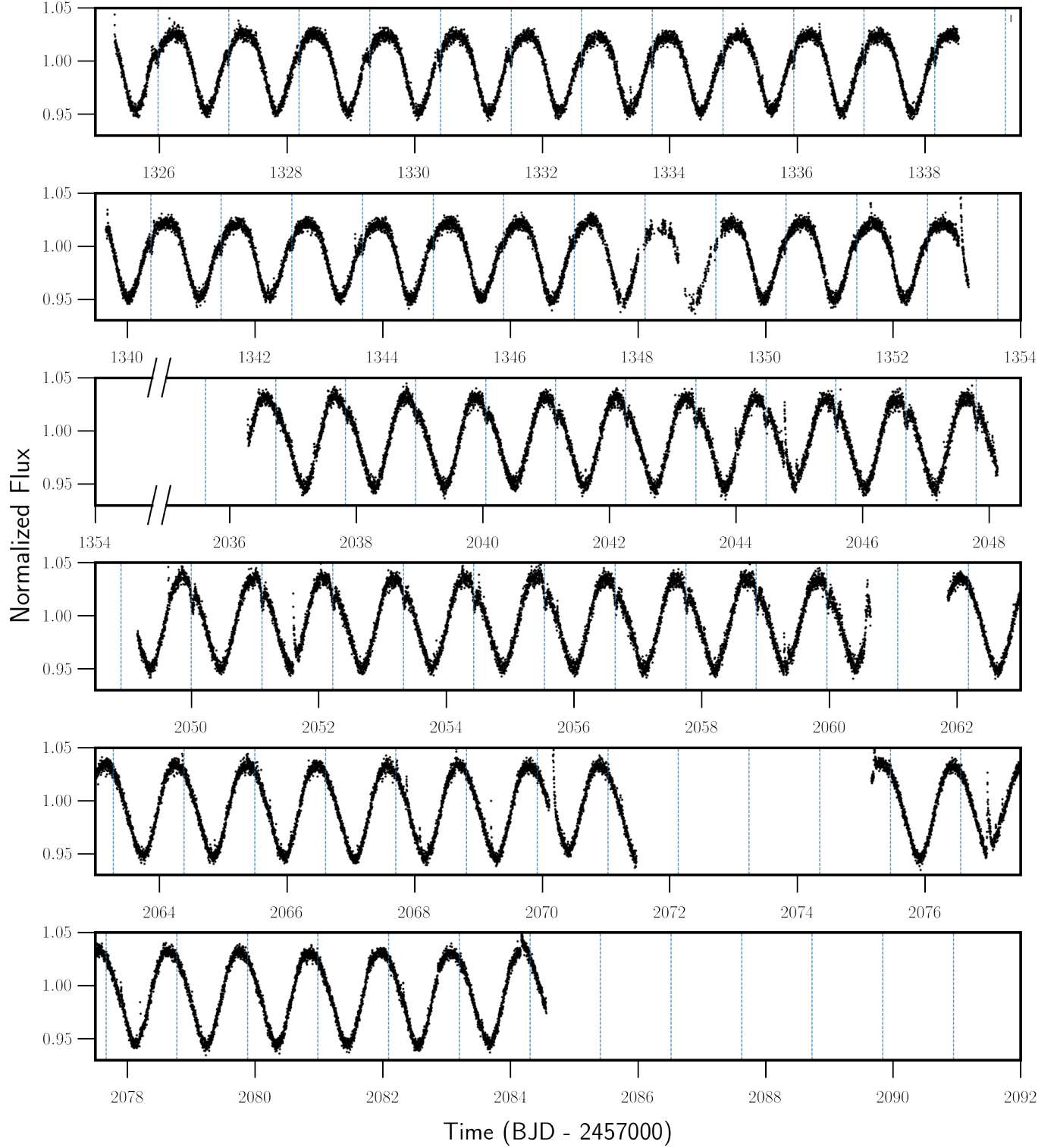


**Figure 3.** Two-minute cadence *TESS* data on TIC 234284556, with data and errorbars in black. Dashed blue lines indicate the anticipated midpoint of each dimming event, projected forward using the rotational period of the star and the midpoint of the first dip in Sectors 1 and 27. The upper limit of the y axis is held at a normalized flux of 1.05, so not all flares are visible in their entirety. The dip disappears quickly between days 2060 and 2062, consistent with centrifugal breakout.

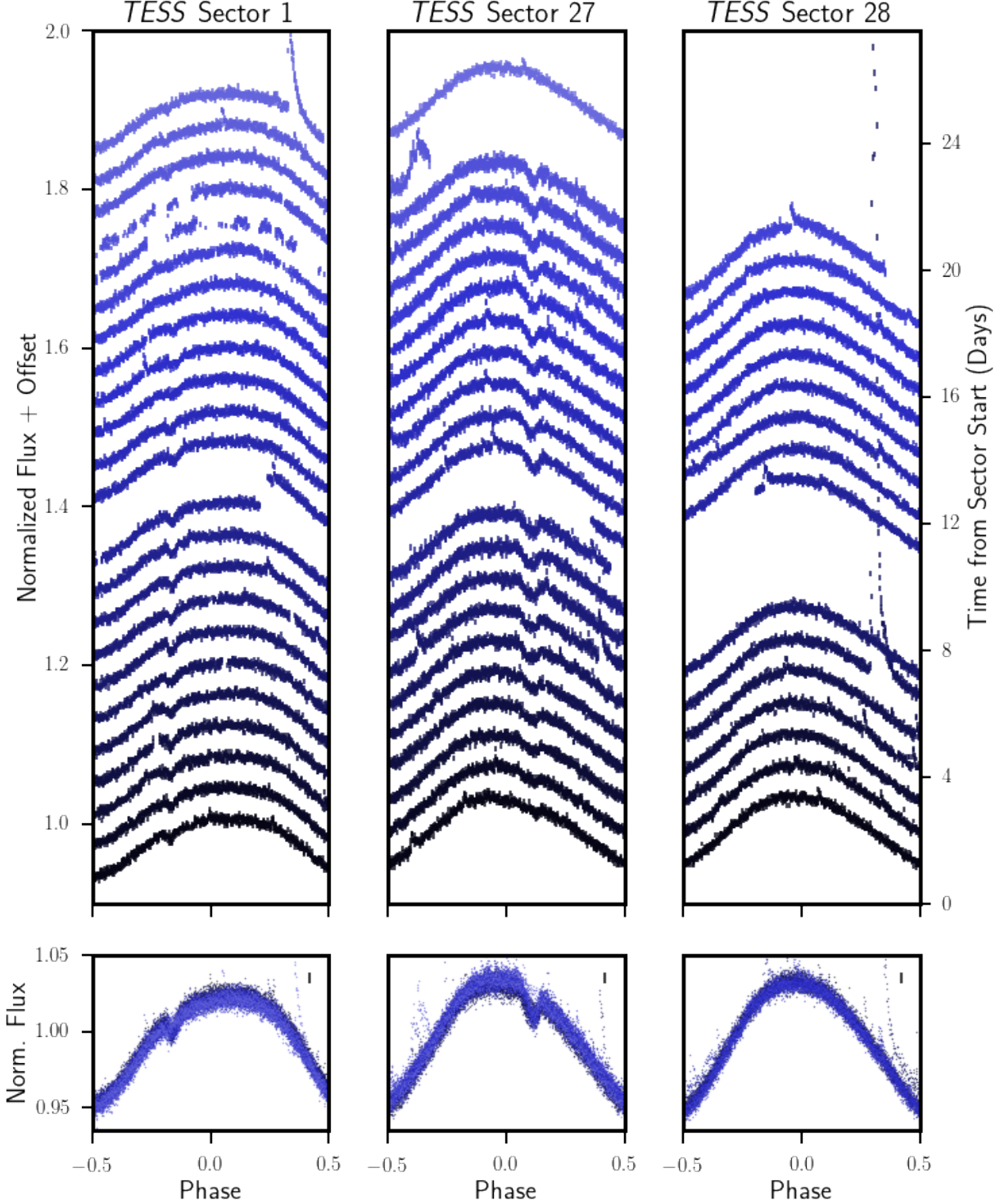


**Figure 4.** *TESS* Light curve folded on the stellar rotation period. The observed dip evolves throughout Sectors 1 and 27, quickly disappearing between Sectors 27 and 28. An unusually symmetric flare-like brightening occurs at the very end of Sector 27, with a  $> 220\%$  flare following some days later in Sector 28. A  $+.04$  vertical offset is added for each new rotational period, so that time progresses upwards on the plot. To emphasize the short timescales involved, the first rotational period of Sector 28 is plotted in the Sector 27 panel.

the signal appears to be astrophysical and related to TIC 234284556.

TIC 234284556 has a strong and roughly sinusoidal rotational signature that is visible in Figures 3 and 4. For a more precise estimate of the period of this rotational signal, we used the `lightkurve` (Lightkurve Collaboration et al. 2018) package’s Lomb-Scargle periodogram to find the maximum of the highest peak of the power spectrum of our star’s rotational signal. Calculating the corresponding uncertainty using the Full Width at Half Maximum (FWHM) of this peak of the power spectrum, we found our target star’s rotational period to be  $1.1066 \pm 0.0003$  days, which is consistent with the  $1.1065 \pm 0.0037$  day orbital period and the  $1.1071 \pm 0.0036$  day stellar rotational period that we inferred from the GP.

In our final data analysis, we took advantage of TIC 234284556’s stable rotational signal to fit a ninth-degree polynomial to the folded, normalized light curve of the two-minute cadence data with the dimming events masked; the polynomial was created using `numpy.polyfit`. After repeating this process for each *TESS* sector, we divided our original data by a periodic version of this polynomial fit to obtain our detrended light curves.

### 2.3. ASAS-SN

TIC 234284556 was also observed by ASAS-SN (Shappee et al. 2014; Jayasinghe et al. 2021), with 208 data points collected over 4.4 years, from 2014 May 12 - 2018 September 24 (HJD 2456789.859 - 2458385.597). There is overlap between the observations of TIC 234284556 during *TESS* Sector 1 and the ASAS-SN data. The uncertainties on and times between ASAS-SN’s measurements are too large for us to claim a detection of a dip during these additional four years of data. However, this data does confirm the stability of TIC 234284556’s rotational period and phase over timescales of years; in particular, the ASAS-SN database (Jayasinghe et al. 2021) reports a period of 1.1066 days, which is consistent with the value we measure from *TESS*.

While the period and phase are consistent over many years, the amplitude observed by ASAS-SN is not. We fit an individual sine wave with a fixed period but amplitude, phase, and a constant offset as free parameters to the five years of ASAS-SN data and to the three sectors of *TESS*. We find that the semi-amplitude of the signal in the ASAS-SN data varies from a minimum of  $2.73 \pm 0.77\%$  in 2014 to a maximum of  $7.45 \pm 0.60\%$  in 2016, as shown in Figure 5. Similarly, the semi-amplitude of the best-fit sinusoid to the *TESS* data varies from  $3.726 \pm 0.007\%$  in Sector 1 to  $4.261 \pm 0.008\%$

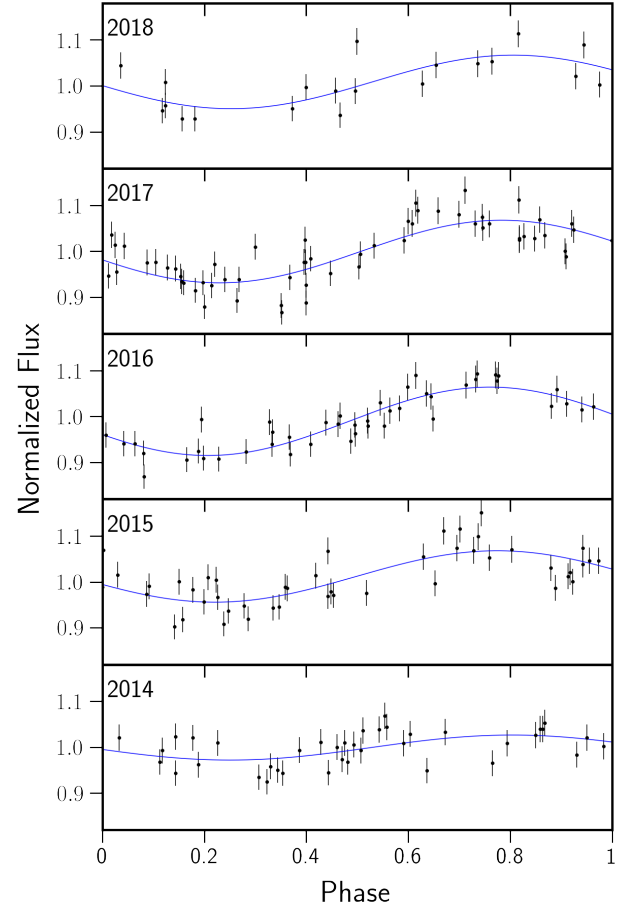


**Figure 5.** ASAS-SN data, labeled by year and shown with the best-fit sinusoid in blue. Note the variation in amplitude from year to year, with the semi-amplitude ranging from  $2.73 \pm 0.77\%$  in 2014 to  $7.45 \pm 0.60\%$  in 2016. This variability indicates that the quasi-sinusoidal signal is driven by starspot evolution rather than Doppler beaming.

and  $4.553 \pm 0.008\%$  in Sectors 27 and 28 respectively. These changes in the amplitude of the star’s variability offer evidence for starspot evolution over the ASAS-SN baseline.

### 2.4. Veloce-Rosso

We observed TIC 234284556 with the Veloce-Rosso spectrograph (Gilbert et al. 2018) at the 3.9-meter Anglo-Australian Telescope of the Siding Spring Observatory over six nights between 2020 October 27 and 2020 November 09. Veloce has a resolution of  $R \approx 80,000$  and, at present, obtains data over the wavelength range 580-930 nm. Our analysis focuses on H $\alpha$ , as further discussed in Section 4.3.

Three of our exposures were taken as 20-minute observations; all other observations were 30 minutes in duration. We used the standard Veloce observing setup from

its planet search program, similar to that of Bouma et al. (2020b). The airmass of these observations ranged from 1.18 to 1.49, while seeing ranged from  $1.^{\prime\prime}7$  to  $2.^{\prime\prime}8$ . In total, we obtained 29 spectra. At wavelengths near  $H\alpha$ , the SNR of these spectra ranges from 10 to 27 per pixel with a mean SNR of 20.

We reduced these data to extract the spectral order containing the  $H\alpha$  line. After removal of the bias level and flat field, we performed a box extraction over a region 49 pixels wide to account for the 19 target fibers corresponding to a  $2.^{\prime\prime}5$  diameter region of the sky centered on our target. Veloce also obtains five sky spectra through offset fibers observed simultaneously, although we note that, at these wavelengths, the sky emission is negligible compared to the brightness of our target star. We infer a wavelength solution from observations of a Thorium-Xenon lamp with the same instrumental setup.

A significant  $H\alpha$  emission signal is present in all 29 spectra obtained with Veloce. Equivalent widths vary over the range  $W_{\alpha} = -5.2$  to  $-9.2$  Å, with the exception of three sequential spectra with  $W_{\alpha} = -11.2$  to  $-12.3$  Å. These values are consistent with the  $W_{\alpha} = -9.40$  Å measured by Kraus et al. (2014) for this star, and broadly fit with the range of equivalent widths measured by Kraus et al. (2014) for young M dwarfs in the Tuc-Hor association and by Scholz et al. (2007) for M dwarfs in the slightly younger  $\beta$  Pictoris moving group.

### 2.5. LCO

We obtained follow-up time-series photometric observations of TIC 234284556 using the 1 m telescopes in the Las Cumbres Observatory network (LCOGT; Brown et al. 2013). The Sinistro cameras mounted on the LCOGT-1m telescopes have a  $26' \times 26'$  field of view, and an unbinned pixel scale of  $0.^{\prime\prime}39\text{ pix}^{-1}$ .

The observations were conducted on the night of UT 2020 November 13 from the SAAO node, with mild defocusing. We opted to use the SDSS  $g'$  filter<sup>4</sup>, based on the expectation that the dips would be chromatic, with the largest depths in the bluest bandpasses (e.g. Onitsuka et al. 2017; Tanimoto et al. 2020; Günther et al. 2020). Ingress and egress were predicted for 18:54 and 20:24 (UT) on the night of based on the *TESS* data. The observations began at astronomical dusk (UT 18:46), continuing until UT 20:53. The full-width at half-maximum of the image point spread function varied

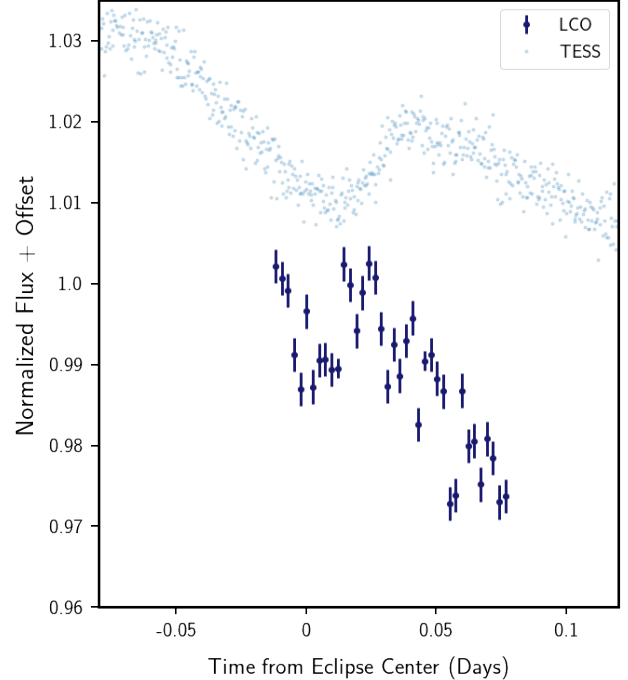


**Figure 6.** LCO follow-up photometry is shown in dark blue with Sector 27 *TESS* data from over 100 days earlier in light blue, providing evidence for the return of a dip over the intervening three months. An offset has been introduced between the two data sets' flux values for ease of visualization. We interpret the different slope of the out-of-transit signal in the *TESS* and LCO data as reflecting observations in different bandpasses.

between  $13.6\text{ pix}$  ( $5.^{\prime\prime}2$ ) and  $17.3\text{ pix}$  ( $6.^{\prime\prime}7$ ), with a median value of  $15.1\text{ pix}$  ( $5.^{\prime\prime}9$ ).

We reduced the images to aperture photometry light curves using the FITSH package (Pál 2012), with the Gaia DR2 catalog used as a reference for determining the astrometric plate solution of each image. We used three concentric apertures for photometry with radii of 15 pix ( $5.^{\prime\prime}8$ ), 20 pix ( $7.^{\prime\prime}8$ ) and 25 pix ( $9.^{\prime\prime}7$ ). The background flux was estimated in an annulus about each aperture with an inner radius of 51 pix ( $19.^{\prime\prime}9$ ) and width of 20 pix ( $7.^{\prime\prime}8$ ). For each aperture, the light curve of the target star had an ensemble correction applied using the other sources in the field as comparison stars. Auxilliary parameters, such as the image position, PSF shape, background, and background deviation were also measured, but, given the uncertainty regarding the expected form for the astrophysical signal that would be present in the observations, we did not detrend against these parameters.

The results are shown in Figure 6. Here, a  $\sim 1$  hour dip of depth  $\approx 15$  mmag appears at the beginning of the observing sequence. Fitting the dip to a transit model

<sup>4</sup> [http://svo2.cab.inta-csic.es/theory/fps/index.php?id=LasCumbres/LasCumbres.SDSS\\_gp&&mode=browse&gname=LasCumbres&gname2=LasCumbres#filter](http://svo2.cab.inta-csic.es/theory/fps/index.php?id=LasCumbres/LasCumbres.SDSS_gp&&mode=browse&gname=LasCumbres&gname2=LasCumbres#filter)

with the same shape as the Sector 27 events but with the depth allowed to vary as a free parameter, we measure a depth of  $1.4 \pm 0.4\%$  in this filter. This event may not be associated with the Sector 27 event given the Sector 28 nondetection. Moreover, since the opacity of the transiting material is likely to have a wavelength dependence, the different bandpasses of the two telescopes can produce apparent depth variations.

With those caveats in mind, we also considered a standard, symmetric transit model following the formalism of [Mandel & Agol \(2002\)](#), which produces a measured eclipse depth of  $1.3 \pm 0.4\%$ . Therefore, either set of assumptions produce a  $3.5 \sigma$  detection of a transit-like event on this night. The detection of this event is significant because the dip was not visible in *TESS* Sector 28, the last month of data collected prior to these LCO observations.

### 3. ANALYSIS

#### 3.1. *Validating the Signal*

In the *TESS* bandpass, TIC 234284556 is 7.3 magnitudes brighter than the closest star ( $28.92''$ ; slightly larger than one *TESS* pixel) and 4 magnitudes brighter than any star within one arcminute. As four magnitudes corresponds to a flux ratio of 40, the rotational signal observed in both *TESS* and ASAS-SN data can only be attributed to TIC 234284556. If this signal were from a background star, it would require at least a 60% obscuration of that star to produce the diluted 1.5% dips observed in *TESS* data, and the periodic signals on two unassociated stars would need to have the same period to within 1-2 minutes, further underscoring the unlikely coincidence needed. Moreover, our LCO follow-up photometry indicates that the dips must be localized to the target star to within  $\sim 2''$ , well within the distance of any resolved sources in the Gaia EDR3 catalog ([Gaia Collaboration et al. 2020](#)), providing additional evidence that the signal indeed belongs to our target star.

#### 3.2. *Eclipse Profiles*

TIC 234284556's dips are visibly asymmetric, with a distinctively triangular shape. (See Figure 7.) To see the asymmetry more quantitatively, we individually performed linear regression on the ingress and egress of the folded, detrended dips in both Sector 1 and 27. Noting that absolute value of the slopes of the Sector 1 ingress and egress ( $0.283 \pm 0.015$  and  $0.216 \pm 0.015$  respectively) are not consistent with each other—and those for Sector 27 ( $0.2425 \pm 0.0059$  and  $0.507 \pm 0.017$  respectively) even more strikingly so. We conclude that there is significant evidence for dip asymmetry in the *TESS* data. Moreover, since the reduced chi-squared of these fits was

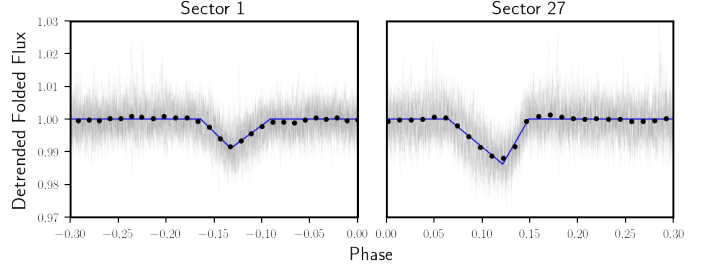


**Figure 7.** Asymmetry of TIC 234284556's dips in Sectors 1 and 27. A section of the full detrended, folded *TESS* data, with error bars, is shown in gray. A binned version of this same data is shown in black. Our best-fit triangular transit model is superimposed in blue. Note the asymmetry of the transit, with the shallower half of the event occurring on the side closest to the maximum brightness of the rotational modulation in both sectors.

lower than 2.3 in each case, it does appear that a triangle is a reasonable fit to this transit.

It is especially interesting to compare these results with the eclipse features of RIK-210 and the transient flux-dip stars. For example, those stars, like TIC 234284556, exhibit asymmetric and triangular transits ([David et al. 2017; Stauffer et al. 2017](#)). In particular, this triangular shape may be taken to suggest that the corotating material has a total extent roughly comparable to the size of their host star. Such a conclusion also matches [David et al. \(2017\)](#)'s estimates for RIK-210, which are based on the observed transit duration.

Interestingly, even with the phase change that occurred from Sector 1 to Sector 27, our dip is in both cases asymmetric in a similar way, with the shallower slope pointed to the peak of the starspot signal. An examination of light curves from other transient flux-dip stars indicates that they also seem to share this feature, hinting that there could be a physical mechanism—potentially related to the corotating plasma tracking magnetic activity—behind this feature. Future work will be needed to understand this in more detail.

#### 3.3. *Changes in Eclipse Parameters*

The light curve shown in Figure 4 indicates that, apart from the sudden disappearance of the dip between Sector 27 and 28 (visible in the center panel), the variation in the depth and duration of TIC 234284556's dips is systematic and gradual. As Figure 4 shows, we also see the signal shift in phase between Sector 1 and Sector 27, indicating either that the orbital period does not perfectly coincide with TIC 234284556's rotational period or that the two signals have different origins.

We now analyze changes in the equivalent duration of the dips present around TIC 234284556. Following

Hunt-Walker et al. (2012), the equivalent duration  $t_{equiv}$  is defined by

$$t_{equiv} = \int_t (F_{norm} - 1) dt, \quad (1)$$

where  $F_{norm}$  is the normalized flux and the dips are integrated over all times  $t$  across their duration. This definition mirrors the equivalent width in spectroscopy, with an integral over time instead of wavelength. Conceptually, the equivalent duration expresses the amount of time that the star's normalized flux would stay at zero in order for the same amount of flux to be blocked as in the actual event that we observe. Thus, the equivalent duration is a proxy for the amount of transiting material, and it is an appropriate choice for our purposes, since—as Figure 4 suggests—the duration, depth, and morphology of TIC 234284556's dips change simultaneously.

To calculate the equivalent duration, we integrated across the dips in our detrended data from Sectors 1 and 27, using the median of the baseline immediately surrounding each dip for improved normalization. Results are shown in Figure 8 and indicate that variations in the equivalent duration are not stochastic, but rather very systematically on  $\sim$ 20-day timescales. Moreover, as the center panel of Figure 4 indicates, we also see potential evidence of drift in the transiting material's orbital period prior to the disappearance of the dip. However, as discussed in Section 5.3, dip duration and morphology changes are difficult to separate out from any possible drift, so we cannot be certain of this conclusion.

### 3.4. Flare Energies and Rate

To identify flares present in the light curve of TIC 234284556, we applied the convolutional neural network (CNN) **stella**, developed by Feinstein et al. (2020b) and trained on flares identified by Günther et al. (2020). The **stella** CNNs allow for flare detection without removing underlying rotational modulation and assigns probabilities to each identified flare being true. Following the methods of Feinstein et al. (2020b), we run and average the probability outputs of 10 CNN models. We included any flare with a **stella**-averaged probability  $> 0.9$ , which indicates the CNN models are 90% confident this is a true flare event. The result of this analysis is presented in Figure 9.

We identified 58 flares across all three *TESS* sectors, visible in Figures 4 and 9. The flare rate was calculated by weighting each flare by the probability assigned by **stella**, which yields a flare rate of 0.74 flares per day. This rate is greater than the average flare rates of young stars (Feinstein et al. 2020b). Assuming a flare temperature of 9000 K and taking  $T_{eff}$  for TIC 234284556 to be

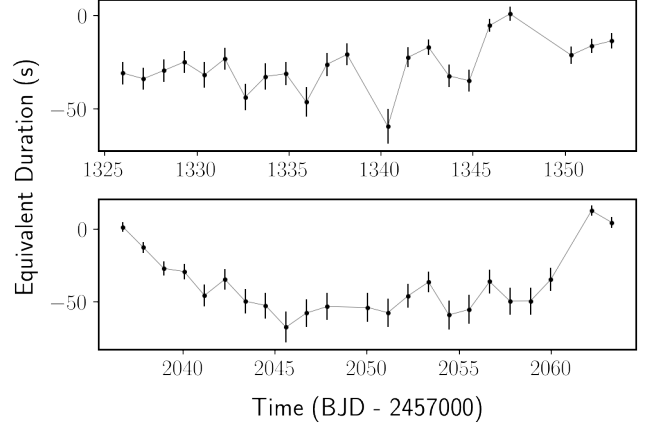


**Figure 8.** Changes in equivalent duration, the time-integrated observed flux decrement and a proxy for the amount of material transiting the star, during *TESS* Sectors 1 and 27. The first two orbits of Sector 28 are shown along with the Sector 27 data. Note the equivalent duration gradually decreases in Sector 1 and increases in Sector 27, followed by the sudden disappearance of any detectable dip between Sector 27 and 28.

3100 K, we find that the flares in the sample span an energy range of  $1.6 \times 10^{32}$  to  $1.3 \times 10^{34}$  erg, with a median energy of  $9.4 \times 10^{32}$  erg. A triple-peaked flare event with an energy of  $3.9 \times 10^{35}$  erg and a measured equivalent duration of 1900.16 s was identified at  $t = 2070.128$  BTJD (Figure 10). A different flare was identified 16 minutes from the phase of the eclipse time projected from Sector 27, but there is no significantly significant relation between the flare occurrence rate and phase overall, as shown in the bottom panel of Fig. 9.

## 4. POTENTIAL ORIGINS OF THE ECLIPSES

In this section, we discuss possible origins of TIC 234284556's dips. We consider in turn the possibility that the dimming events are caused by a disintegrating or sublimating planet, a precessing planet, a planet transiting an active stellar surface, an eclipsing black hole-M dwarf binary, secondary eclipses of slingshot prominences, or transiting magnetospheric clouds. Considering these possibilities in the context of our observations, we then argue that, of these scenarios, only magnetospheric clouds are a plausible origin of the dips.

### 4.1. A Planetary Origin

#### 4.1.1. A Disintegrating or Sublimating Planet

The variation in TIC 234284556's eclipse characteristics over timescales of days is a distinguishing features of this system. Beyond the sudden disappearance of the dip over the course of one rotational period between Sectors 27 and 28, there are changes in the depth, du-

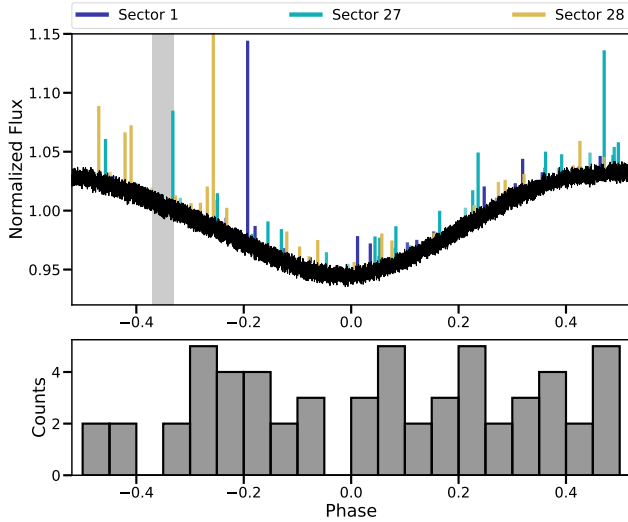


**Figure 9.** Results of the `stella` CNNs run on the three light curves of TIC 234284556. Top Panel: Distribution of flares over a phase folded light curve for TIC 234284556. Flares are scaled by the amplitude of the flare and are colored by the *TESS* sector they were observed in. The gray shaded region highlights the phase at which the dip is located. The upper limit of the y axis is held at a normalized flux of 1.15, so the largest flare in Sector 28, as shown in Figure 10, is not visible in its entirety. Bottom Panel: A histogram representation of the number of flares identified at each rotational phase. Flares are binned in  $\Delta$  Phase = 0.05. There is no evidence for a correlation between flare rates and rotational phase.

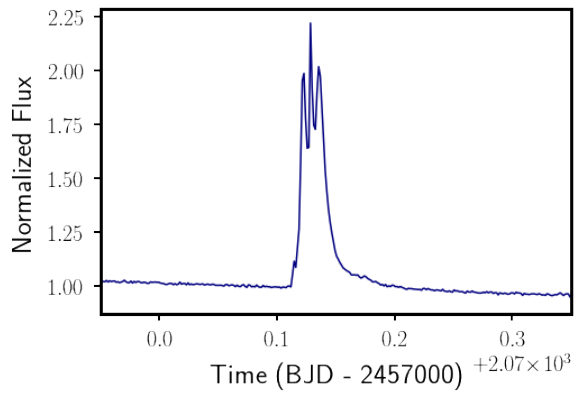


**Figure 10.** The  $\approx$ 220% triple flare in the *TESS* bandpass that appears in Sector 28, days after the disappearance of the dip. This may be interpreted as additional evidence for increased magnetic activity in the time surrounding the potential centrifugal breakout event.

ration, and morphology of the dips throughout Sectors 1 and 27. (See Figures 4 and 8.)

There is precedent for changes in dip parameters even in planetary transits, for example among disintegrating

planets, planets that gradually lose mass via a stream of dusty material as they are consumed by their host star (e.g. Sanchis-Ojeda et al. 2015; Vanderburg et al. 2015). However, the known disintegrating planets have somewhat shorter periods, ranging from 4.5 to 22 hours (Lieshout & Rappaport 2018; Vanderburg et al. 2015)), more extreme and stochastic depth variations (Rappaport et al. 2012) and a pre- and/or post-ingress bump that may be ascribed to the scattering of light (Rappaport et al. 2012; Sanchis-Ojeda et al. 2015).

Our system does not exhibit any of these characteristics and, in particular, the gradual change in equivalent duration that we see in Figure 8 does not match the expectation for stochastic variations in the geometric arrangement of transiting dust. Moreover, our lower bound on the Roche Limit, obtained by conservatively assuming a planet density of  $0.5 \text{ g cm}^{-3}$ , is  $5.3 \times 10^{10} \text{ cm}$  as compared to a co-rotation radius of  $2.4 \times 10^{11} \text{ cm}$ . Based on these arguments, the dips in the light curve of TIC 234284556 are inconsistent with the presence of a disintegrating planet.

We next consider the possibility that the dips are instead caused by a sublimating planet. Following methods presented in David et al. (2016), and using values from Table 2, we estimate the  $T_{\text{eff}}$  of material at the co-rotation radius to be  $T_{\text{corot}} = 806 \pm 41 \text{ K}$ . The transiting material is thus below the sublimation temperatures of olivine, pyroxene, and carbon, although likely above the sublimation temperature of iron (Kobayashi et al. 2011). This implies that the signal is likely not from the sublimation of a planet with an Earth-like composition, although a strictly iron core could in principle be sublimating. However, this scenario would not cleanly explain the co-rotation between the orbiting material and the stellar rotation or the phase change from Sector 1 to 27. Moreover, from Sector 28 data, we can rule out a dip deeper than 400 ppm, and therefore the presence of a planet bigger than  $0.9 R_{\oplus}$ , with 95% confidence. Hence, any material that we observe in Sector 27 is dominated by a component other than an opaque transiting planet, if one exists in the system.

#### 4.1.2. A Precessing Planet

A precessing planet is a planet that is being torqued in and out of our line of sight by a massive object; this is another possible cause of the depth-varying dips that we observe, particularly since the dip disappears in *TESS* Sector 28. However, transits of precessing planets vary over timescales around two orders of magnitude larger than what is seen for TIC 234284556. For example, PTFO 8-8695, if explained as a transiting planet, is thought to have a precession period of 293 days or

581 days (Barnes et al. 2013). Meanwhile, K2-146, a mid-M dwarf with two transiting planets, shows extreme transit-timing variations and has an estimated nodal precession period of 106 years (Hamann et al. 2019). Since the dip disappears over a  $\sim$ 1-day timescale, precession alone cannot explain the sudden disappearance of the dip between Sectors 27 and 28. Additionally, a precessing planet does not neatly explain the match between the orbital and rotational periods or the phase change of the signal from Sector 1 to Sector 27.

#### 4.1.3. A Planet Transiting an Active Stellar Surface

Another possibility is that the dips originate from a planet transiting an active latitude on TIC 234284556. Under this scenario, the planet’s transit chord would block a region on the stellar surface that has variable flux. For example, Sector 1’s gradual decrease in the dip depth over time could correspond to a planet that is transiting across a band of starspots, where that band is gradually growing to cover a larger fraction of the star’s surface over time; Sector 27’s increase in dip depth would then correspond to a decay of a similar band.

For this situation to explain the transit duration variations that we observe in Sector 1 and 27, there would need to be a sharp boundary between the active region and the quiet region on the star. Otherwise, we would observe a dip that continues to have a consistent duration (due to the fixed size of the planet), despite varying depth during and between transits. Moreover, the gradual changes in dip equivalent duration that we observe (Figure 8) over the course of Sectors 1 and 27 imply that the active region must be moving slowly across the stellar surface. Finally, since we do not observe significant changes in the spot signal over the sector, the active band would likely have to be rotationally symmetric, and therefore an active latitude.

However, the sudden disappearance of the dip at the Sector 27 to 28 boundary implies that this hypothetical active region would have to grow from a near-minimum state to its maximum state within a  $\sim$ 1-day timescale—at odds with the slow growth required to explain the changing dip parameters in Sector 1 and 27. Moreover, given that we do not see any change in the rotational signal, this scenario would require that the rapid growth of the active latitude occurs uniformly, across all longitudes of the star. Long-term ASAS-SN data does not give any evidence for step-function magnitude changes at this level, so we can disfavor this model.

#### 4.2. A Compact Companion

In principle, the stable and strong sinusoidal signal that we have, until now, attributed to TIC 234284556’s starspots could instead be explained by relativistic

Doppler beaming. In this scenario, light emitted isotropically in a moving object’s reference frame becomes concentrated when moving towards an external observer and fainter when moving away, leading to an ellipsoidal modulation in the light curve (e.g. Mazeh & Faigler 2010; Faigler et al. 2013).

To first order, the amplitude of the beaming signal is proportional to  $4K/c$ , where  $K$  is the orbital Doppler semi-amplitude and  $c$  the speed of light. In the context of our system, beaming would require TIC 234284556 to be a binary system with a black hole. Under this scenario, the transit-like signal would be caused by the secondary eclipse of TIC 234284556 by its compact companion, and the changing dip parameters could be explained due to varying levels of accretion onto the black hole.

We reject the compact companion hypothesis for two reasons. First, Doppler beaming would require an unchanging sinusoidal signal because the binary system would be expected to have fixed orbital parameters that would lead to a perfectly repeatable beaming effect. This is not, however, consistent with our observations. As described in Section 2.3, the observed amplitude varies by more than a factor of two from year to year, suggestive of starspot evolution and inconsistent with Doppler beaming.

Moreover, if TIC 234284556 were in a binary system, we should have seen evidence of that in our Veloce data. However, we do not observe km/s variability in the spectra, despite the fact that Veloce would have been sensitive to a Doppler signal with that amplitude. Hence, we can effectively rule out both the presence of a compact companion and this scenario for the origin of the dips.

#### 4.3. Secondary Eclipses of Slingshot Prominences

Slingshot prominences are cool, dense, co-rotating clumps of gas that are trapped along coronal field lines (Jardine & Collier Cameron 2018). Prominences are especially common around stars with strong magnetic fields, such as young M dwarfs (Jardine & Collier Cameron 2018) like TIC 234284556. Importantly, the slingshot prominence model has an associated mass-loss mechanism that is analogous to centrifugal breakout of trapped corotating material; we could potentially use such a mechanism to explain the sudden disappearance of the dip between *TESS* Sectors 27 and 28. According to the model presented in Jardine et al. (2019), slingshot prominences will continue to grow until the accumulated mass exceeds the limit of what the star’s magnetic field can constrain. At this point, the co-rotating material will be expelled.

In the slingshot prominence model, the dips are caused by corotating plasma that is emitting in specific spectral lines; when this plasma passes *behind* the star, there is a decrease in the flux that we observe. One prediction of this model, would be extreme variations in the shape of H $\alpha$  as this plasma rotates across the stellar surface. These variations manifest themselves as changes in the line profile via the Rossiter-McLaughlin effect, as the blue-shifted and then red-shifted hemisphere of the rotating star is obscured in turn (Rossiter 1924; McLaughlin 1924).

However, considering that our LCO data's bandpass is bluer than 656 nm and comparing the width of the TESS bandpass with the  $-5.2$  to  $-9.2$  Å equivalent width range from Veloce (See Section 2.4), it seems that some other source of emissivity beyond H $\alpha$  would be necessary to account for the observed depth of the dip under the slingshot prominence scenario. In analogy with David et al. (2017)'s reasoning for RIK-210, we conclude that Paschen-continuum bound-free emission could produce broadband dimmings of up to a few percent—deep enough to produce our observed dips around for TIC 234284556, although insufficient to explain RIK-210's dimmings.

As described in Section 2.4, we observe a significant H $\alpha$  emission signal over all 29 spectra obtained with Veloce. The observed variability, shown in Figure 11, is largely coherent with the rotational modulation due to starspots, with a larger equivalent width observed when the starspot coverage in the visible hemisphere is higher. However, the seven observations from UT 2020 November 03 provide an exception to this trend. On this night, seven spectra were obtained: four spanning two hours and three additional spectra obtained after a 45-minute gap, spanning 90 minutes. The three spectra after the gap all exhibit an equivalent width in the H $\alpha$  line more than 20% larger than any other feature. Moreover, during these three exposures the feature has an extended blue-shifted component with a velocity of 30-50 km/s.

This behavior is morphologically similar to spectroscopic signatures of flares (Honda et al. 2018; Maehara et al. 2021). In principle, it could also be emission from a co-rotating blue prominence; there is a gap of at least three days before and after these spectra were obtained. This would correspond to a shorter event timescale than those observed in Sectors 1 and 27 of *TESS*, but without simultaneous photometry we cannot rule out this scenario.

However, given the high flare rate for this star and the lack of line profile variations in the core of the H $\alpha$  line for any spectra obtained over this 13-night baseline, we find a stellar flare to be the most plausible expla-

nation of the increased equivalent width and blueward asymmetry on these nights. With that caveat, there is no significant change in the shape of the H $\alpha$  feature in time, a result which is counter to predictions for a slingshot prominence (e.g. Zaire et al. 2021). The stability of the shape of the H $\alpha$  line, which we'd expect to be mirrored in a similar stability of the Paschen lines, thus suggests a different mechanism than the slingshot prominence model.

#### 4.4. *Transiting Magnetospheric Clouds*

Like slingshot prominences, magnetospheric clouds consist of material originating from the star that gets trapped in the host star's magnetosphere. However, the effects of eclipsing slingshot prominences would be primarily driven by hot plasma (Waugh et al. 2021), whereas transiting magnetospheric clouds trap dust as well as ionized hydrogen, leading to additional opacity visible in broadband photometry (e.g. David et al. 2017). Since only a small amount of dust is needed to create significant optical dimmings, a magnetospheric cloud's photometric signature can occur during a transit rather than during a secondary eclipse.

As with slingshot prominences, magnetospheric clouds would produce a signal with a period matching the rotational period. As material fills and seeps out of the magnetically-confined region of material, the depth of the eclipses can vary over time. As the material is gas and dust grains, it will have a relatively weak wavelength dependence compared to the strong spectral signature of a plasma in the slingshot prominence scenario. These predictions match the variable light curve and unchanging line profile variations observed in this data set, making this scenario our preferred explanation for the observed behavior of TIC 234284556.

For RIK-210, a potential younger analog of TIC 234284556, David et al. (2017) also preferred the magnetospheric cloud model over the slingshot prominence model, finding that eclipses of prominences could not explain RIK-210's 20% deep dips in the Kepler bandpass. Although the dip depth of TIC 234284556 ( $\leq 1.2\%$ ) is not large enough to conclusively rule out the slingshot prominence scenario on these grounds, the observed lack of variability in the H $\alpha$  line profile still gives us reason to prefer the magnetospheric cloud scenario over the slingshot prominence model.

If the signal observed in this system is indeed the result of magnetospheric clouds, then we require an explanation of how sufficient material can become trapped in the magnetosphere of TIC 234284556 and of how this material can dissipate over the 1-2 rotation periods be-

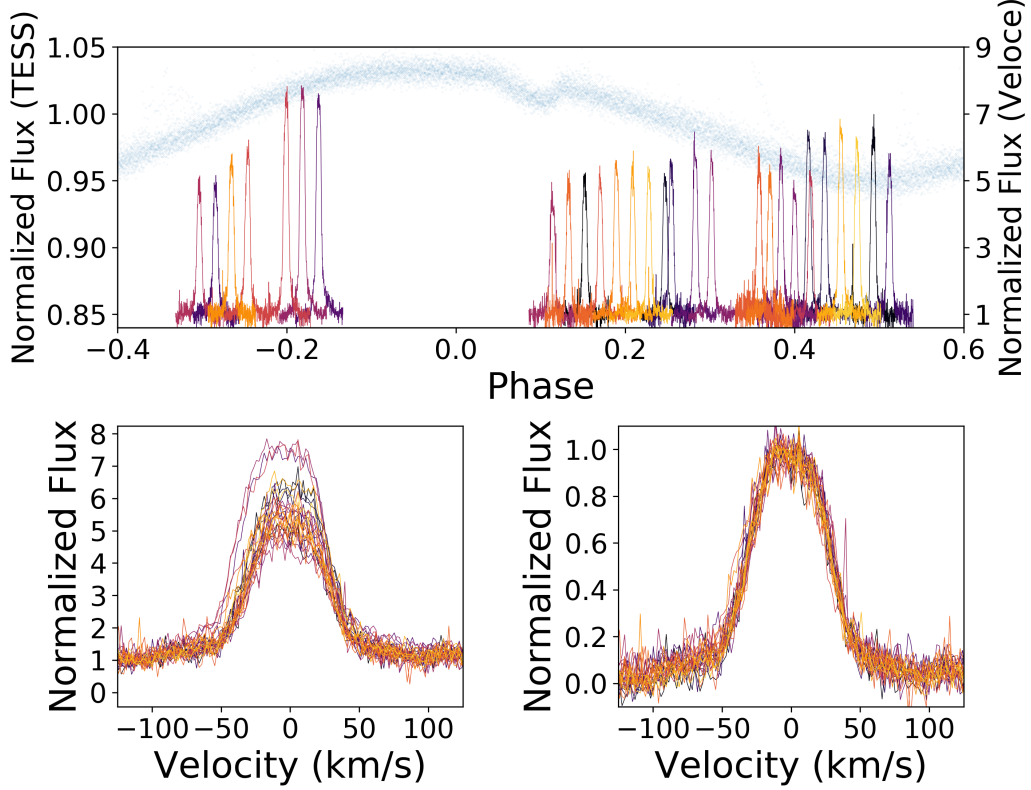


**Figure 11.** (Top) Phase-folded light curve for Sector 27, with normalized H $\alpha$  spectra plotted at the phases of observations. (Bottom left) The same H $\alpha$  spectra, overplotted. There is no significant shape variations over this spectral feature, leading us to disfavor the eclipsing slingshot prominence scenario. For both frames, colors progress in time across all observations, shifting from black to purple to red to orange to yellow as the night moves on. The amplitude of this feature varies with starspot coverage as is typical for young stars. There are three spectra, observed sequentially, with significantly larger amplitudes and excess emission at blue wavelengths compared to all other observations; we attribute this variability to a potential flare event on this star during these observations. (Bottom right) The same as the previous subfigure, with all spectra excluding the three belonging to the flare candidate normalized to the same amplitude and equivalent width to demonstrate no significant shape variations over the remaining observations.

tween Sectors 27 and 28. These are discussed in turn below.

## 5. CENTRIFUGAL BREAKOUT

### 5.1. *The Case for Breakout*

Perhaps the most distinguishing feature of TIC 234284556’s dips is their sudden disappearance over a  $\sim$ 1 day timescale. Immediately prior to the disappearance of the dip, we observe a flare-like event with an unusually symmetric morphology (See Figure 12 and Section 2.2). Moreover, in the days surrounding the dip’s disappearance, we see additional evidence for increased magnetic activity, including a  $\approx$ 220% triple flare some days after the potential breakout event as well as a higher amplitude variability of the starspot signal in Sectors 27 and 28 as compared to Sector 1 (See Figure

10). In addition to the dip’s sudden disappearance, we also see evidence of variability on top of a rotational signal that is strong and stable over timescales of years. In particular, we see systematic variations in the the equivalent duration of TIC 234284556’s eclipses (See Figure 8 and Section 3.3), a phase change of the seemingly corotating dip from Sector 1 to Sector 27, and a reappearance of the dip in our LCO data.

All of these data are consistent with a magnetospheric cloud/centrifugal breakout model. The short timescale involved in the dip’s disappearance is plausibly explained a sudden snapping of the star’s magnetic field lines when the mass of the corotating material exceeds TIC 234284556’s capacity to restrain it, whereas the alternative mass-loss mechanisms discussed in Section 6.2 would predict longer timescales. Meanwhile,

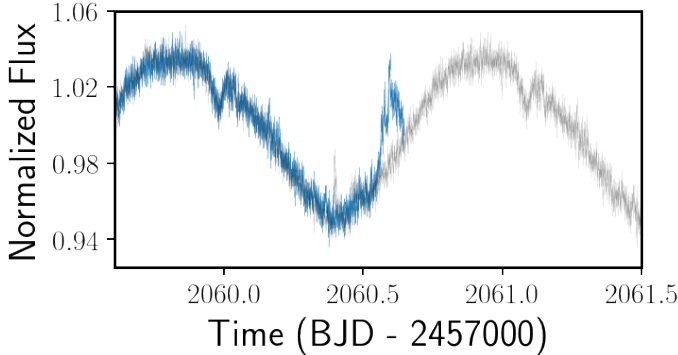


**Figure 12.** *TESS* light curve at the end of Sector 27 (Blue), with an observed brightening at the end of the sector. For comparison, the light curve one rotational period earlier is underlaid (Gray). Note that this brightening event has a symmetric morphology unlike the steep rise and exponential decline typical of stellar flares. We consider this feature a potential post-breakout magnetic reconnection event, highlighting that the potential analogs of TIC 234284556 discussed in Stauffer et al. (2017) also exhibited symmetric flare-like events at state transitions.

the heightened magnetic activity around the time of the dip’s disappearance would also be expected from centrifugal breakout and the unusually symmetric flare-like event that coincides with the dip’s disappearance (Figure 12) could plausibly be a post-breakout magnetic reconnection event.

In support of this last point, the existing theories of stellar magnetism predict that magnetic reconnection events could resemble flares (Townsend et al. 2013; Stauffer et al. 2017), although a link between optical flaring and reconnection events specific to centrifugally supported magnetospheres has yet to be definitively established (Townsend et al. 2013). Suggestively, like TIC 234284556, some of the persistent flux-dip stars and scallop shell stars had unusually symmetric flare-like events that occurred at state transitions (Stauffer et al. 2017). Since these state transitions and the corotating cloud origin promoted by Stauffer et al. (2017, 2018, 2021) fit many of the same criteria for centrifugal breakout that TIC 234284556 does, this correlation between symmetric flares and major changes in the dip properties could be taken to be an indication of the magnetic reconnection events that are expected to occur immediately after the magnetic field lines are broken during a breakout event.

Moreover, the physical mechanism of centrifugal breakout fits with the magnetospheric cloud dip origin that Section 4 found to be the most probable, and TIC 234284556’s rotational signature indicates that the star does, in fact, have a strong and stable magnetic field — one of the prerequisites for a corotating magneto-

sphere. Furthermore, the systematic variations observed in the equivalent duration of TIC 234284556’s transit-like events (See Figure 8 and Section 3.3) is one of the indicators of breakout that Townsend & Owocki (2005) sought in their non-detection of centrifugal breakout around  $\sigma$  Ori E. And, finally, multiple breakout events with the material subsequently being replenished by the star can explain the corotating dip’s phase change — the magnetic field topology of the star could plausibly have evolved over the course of years, leading to a change in the preferred location for the dip — as well as the LCO data’s evidence for the reappearance of the dip.

All things considered, due to a combination of a strong consistency of our data with the predictions of centrifugal breakout and a lack of plausible alternatives to this explanation, we claim that centrifugal breakout is the most compelling explanation for the sudden disappearance of the dip.

## 5.2. Constraining the Pre-Breakout Mass

Appendix A2 of Townsend & Owocki (2005) estimates the asymptotic mass, or mass required for breakout to occur as

$$m_\infty \approx \frac{\sqrt{\pi} B_*^2 R_*^4}{6 g_* r_K^2} \quad (2)$$

where  $B_*$  is the strength of the star’s magnetic field,  $R_*$  is the radius of the star,  $g_*$  is the star’s surface gravity, and  $r_K$  is the Kepler corotation radius.

If future observations measure TIC 234284556’s magnetic field, we will be able to calculate the theoretically-predicted asymptotic mass directly and compare that to the observed depth of the dip immediately prior to breakout. We do not currently have a good understanding of TIC 234284556’s magnetic field strength, however, so here we use an approach inspired by Boyajian et al. (2016) to estimate a lower limit for the mass of dust present immediately before the possible breakout event from the depth of the dip. We then make an order of magnitude approximation of the total mass of transiting material, based on the mass of optically thick material.

First, borrowing Equation 4 from Boyajian et al. (2016), we use the relation

$$\sigma_{\text{tot}} = v_t h \int \tau(t) dt \quad (3)$$

to estimate the cross-sectional area  $\sigma_{\text{tot}}$  of the optically thick corotating material. Here,  $v_t$  is the transverse velocity of the material,  $h$  the height of the material perpendicular to its velocity, and  $\tau(t)$  the optical depth as it changes over the course of a rotational period.

For  $h$ , we assume a spherical shape for the corotating material and use 1.2% as the approximate depth

of the last dip in Sector 27. For  $v_t$ , we assume uniform circular motion so that  $v_t = 2\pi a/P$ , where  $P$ , the orbital period of the material, coincides with TIC 234284556's rotational period and the orbital radius  $a$  of the material can be computed from Kepler's third law. Finally, to approximate  $\int \tau(t) dt$  for the dip immediately prior to breakout, we use the approximation that  $\tau \approx \ln(\text{normalized flux})$ . We detrend the normalized light curve as described in Section 2.2 and then integrate numerically over the dip. In this way we find that  $\sigma_{\text{tot}} = 4 \times 10^{14} \text{ m}^2$ .

As in Boyajian et al. (2016), we calculate a lower limit for the mass of dust transiting the star that is given by

$$M_p = \frac{2}{3} \sigma_{\text{tot}} \rho D \quad (4)$$

where we take the dust grains to be made of particles with a uniform density  $\rho = 3 \text{ g cm}^{-3}$  and diameter  $D = 1 \mu\text{m}$ .

In this way, we would obtain an obtain an equivalent radius of 410 m if all of the dust were gathered into a sphere with density  $3 \text{ g cm}^{-3}$ , and we estimate a dust mass of  $9 \times 10^{14} \text{ g}$ . However, the mass of the transiting material is likely dominated by transparent plasma, not by the dust that contributes to opacity. Although we do not have tight constraints on the plasma-to-dust ratio, it is typical for a protoplanetary disk to be 99% gas and 1% dust, and for a star to be 98% Hydrogen and Helium and 2% metals by mass. Hence, for a first-order approximation, we take 1.5% of the total mass to be optically thick, which gives us an estimate of  $6 \times 10^{16} \text{ g}$ —about a quarter the mass of Halley's comet—for all of the transiting material.

This demonstrates that, in principle, a very small amount of mass could cause the observed dip. However, we emphasize this is a lower bound on the mass. In producing this estimate, we have assumed that we have seen the entire cloud transiting, and we also do not have well-constrained estimates for the spatial distribution, diameter, and density of the transiting material. Further underscoring this point, if we tentatively assume that this will coincide with the asymptotic mass (as calculated using equation A11 from Townsend & Owocki 2005) we would arrive at the an estimate of 0.03 kG for TIC 234284556's magnetic field strength, comparable to that of the Sun. However, a magnetic field at least a factor of three larger, from 0.1 to 10 kG (Gregory et al. 2012; Shulyak et al. 2019), would better align with expectations for a young, low-mass star, suggesting that either we are only seeing a small fraction of the plasma transit or else that the dipole-dominated magnetic model assumed by Townsend & Owocki (2005) does not hold for this star.

### 5.3. Asynchronicity of the Signal

So far, we have presented the the transiting material as likely to be corotating with the star. After all, the period of TIC 234284556 falls within our one sigma confidence interval for the period of the dip. However, as Figure 13, a river plot of the three sectors of *TESS* data, shows, the transit midpoint appears to start to falling behind the predicted ephemeris as time goes on. It is not clear if this apparent drift is best explained by a change in dip duration or as a genuine change in the orbital period. In fact, even as the ingress and transit midpoint in Sector 27 begin to lag, the egress remains at a relatively constant phase throughout the sector.

If we take this apparent drift at face value, this would correspond to 16 minutes of drift over the course of Sector 27, with a similar, though less pronounced, phenomenon occurring during Sector 1. This corresponds to a difference of less than one minute between the rotational and orbital periods. In the context of centrifugal breakout, such a drift in period could be interpreted as evidence of material gradually drifting outwards and dragging the magnetic field lines behind it until the field lines snap at the time of a breakout event. However, once again, dip duration and morphology changes are difficult to separate out from any possible drift, so we cannot be certain of this conclusion.

## 6. DISCUSSION

### 6.1. Toward Timescale Estimates

The evolution of TIC 234284556's dips appears to be governed by changes occurring on three different timescales:

1. The disappearance of the dip, which, for TIC 234284556, occurs on a  $\sim$ 1-day timescale.
2. Changes in the depth, duration, and shape of the dip, seemingly on a  $\sim$ 10-day timescale
3. The post-breakout reappearance of the dip, poorly constrained by our current data, but occurring no more slowly than on  $\sim$ 100-day timescales.

In particular, we suspect that our current data on TIC 234284556 corresponds to a minimum of three distinct dips, with one change inferred from the shift in the phase of the corotating plasma from Sector 1 to Sector 27, and another from the dip detected in the LCO data 107 days after the dip disappeared between Sectors 27 and 28. Importantly, we have no lower bound on the timescales involved in the post-breakout reappearance of the dip—and we would need such information in order to distinguish between the CME and stellar wind

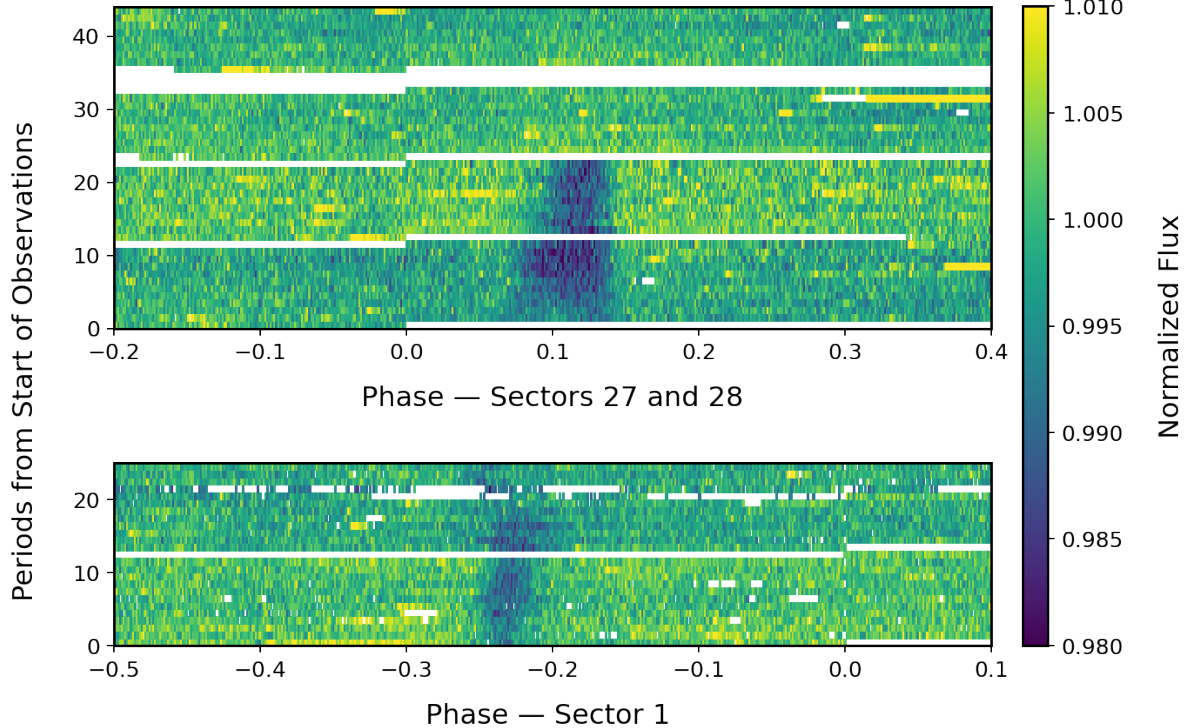


**Figure 13.** River plot of *TESS* data phased to the stellar spin period of 1.1066 days and with the rotational signal removed. There is an observed drift of the transit midpoint and the transit duration changes from event to event. The sudden disappearance of the dip between Sector 27 and 28, which corresponds to the potential breakout event, is also apparent.

mass-accumulation scenarios that are presented in Section 6.3.

The timescales for the disappearance of the dip and for the dip depth, duration, and morphological changes appears to be broadly consistent with those for the transient flux-dip stars from Stauffer et al. (2017). Notably, however, for TIC 234284556 we have a two year baseline over which the dips are observed, which is important for understanding the longer-term evolution of this type of star. In particular, in these two years of data, we see a phase change, with the dip in Sector 27 offset in phase from the dip in Sector 1 by 29% of an orbit—something observed in PTFO 8-8695 and TIC 234284556, but not in any of the other known transient flux-dip stars.

## 6.2. Mass-Loss Mechanisms

Ever since Townsend et al. (2013) found a lack of photometric evidence for centrifugal breakout around  $\sigma$  Ori E, astronomers have been considering alternate mass-loss mechanisms for plasma accumulated in a centrifugal magnetosphere. In particular, Owocki & Cranmer (2017) presented a diffusion-drift model in which plasma escapes away from the star via diffusion and drift, and toward the star via diffusion. However Shultz et al. (2020), after examining early B stars that are

candidates for a centrifugal magnetosphere and finding that their  $H\alpha$  emission profiles favor centrifugal breakout over the diffusion and drift model, proposed that centrifugal breakout is the relevant mass-loss mechanism, but that it essentially acts as a leakage mechanism. Responding to Shultz et al. (2020), Owocki et al. (2020) argued that diffusion-drift may still be an important mechanism for late-B and A-type stars, because the much weaker winds of these less massive stars would not allow their centrifugal magnetospheres to fill the level needed for breakout.

We argue that TIC 234284556 and a handful of the stars described in Stauffer et al. (2017) provide strong supporting evidence for the centrifugal breakout model. They complement the spectroscopic and theoretical case for centrifugal breakout with the evidence of specific light curves, where, crucially, photometric nondetections were what first led to doubts about centrifugal breakout's importance. In particular, considering the sudden disappearance of the dip, the centrifugal breakout candidate that we observe cannot be governed by purely continuous centrifugal leakage of the kind proposed by Shultz et al. (2020).

However, centrifugal breakout alone does not explain the gradual decrease in dip size observed in Sector 1, sug-

gesting that there may still be a role for an additional mass-loss mechanism. Although we cannot exclude a centrifugal leakage-based explanation, we consider that the corotating material will only interact with the stellar magnetic field when the dust is hot enough to stay ionized. This will be the case while stellar flares continue to heat the corotating material. However, if TIC 234284556 enters a quiescent period, the dust will begin to undergo recombination and the apparent dip will decay. This flaring mechanism seems plausible because the work function of circumstellar dust is on the order of  $\sim 5$  eV (Tielens 2005), and a study by Howard et al. (2020) indicated that even 20000 K flares may not be uncommon around low-mass stars, making flares a plausible source of the ultraviolet photons needed for ionization. Moreover, Osten et al. (2013) propose a similar mechanism in their paper. In the context of TIC 234284556, we note a lack of major flares in the second orbit of Sector 1 (see Figures 9 and 4), at the time of the decay in observed dip size, consistent with the model proposed here.

### 6.3. Stellar Winds or CME?

There is one important reason for caution in generalizing our interpretation of TIC 234284556’s data to other stars: its low mass. TIC 234284556 is a  $0.42 M_{\odot}$  M3.5 star, whereas the theory behind centrifugal breakout and the spectroscopic evidence takes place in the context of high-mass (A- and B-type) stars. Although centrifugal breakout should proceed in the same way regardless of the trapped material’s origin, the mechanism for filling the magnetosphere may need to be different for an M dwarf. In fact, for massive stars, the assumption is that stellar wind is the source of the plasma trapped in their centrifugal magnetospheres, but an M dwarf’s stellar wind may not supply enough material for the asymptotic mass to be reached.

For low-mass stars, the mass-loss rates from stellar wind  $\dot{M}_{wind}$  are very difficult to constrain; estimates in the literature differ by nearly five orders of magnitude, ranging from  $4 \times 10^{-15} M_{\odot} \text{ yr}^{-1}$  to  $10^{-10} M_{\odot} \text{ yr}^{-1}$  (Vidotto et al. 2013). Moreover, in recent years, it has been suggested that, among young stars, the mass-loss from CMEs  $\dot{M}_{CME}$  may dominate over the outflow from stellar wind (Jardine & Collier Cameron 2018), possibly by one to two orders of magnitude, for a solar mass star in its first 300 million years or so (Cranmer 2017). Even more suggestively, Alvarado-Gómez et al. (2018)’s simulations of low-mass star CMEs indicated that a strong dipolar magnetic field prevents CMEs from breaking free from their stars.

Our current data on TIC 234284556 is consistent with both the CME and stellar wind scenarios. As we demonstrated in Section 6.2, the observed dip depth could theoretically be caused by a small amount of mass, in which case stellar winds are still be a plausible explanation, but the low (0.03 kG) magnetic field strength predicted from that mass could give us reason to favor a higher mass estimate, and future data may more tightly constrain the timescales involved in accumulating the asymptotic mass. Observationally, our LCO data already offers us an upper bound on the timescales involved in the post-breakout reappearance of the dip, but the 107 days between the last *TESS* dip and the LCO dip is too large for us to eliminate either the stellar wind or the CME scenario, and we would need a magnetic field measurement to get a theoretically-motivated estimate of the mass that has accumulated immediately prior to breakout.

Future observations of TIC 234284556 may offer us a unique way to constrain the mass-accumulation rate and to clarify the relationship between magnetospheric clouds and CMEs. For example, if the reappearance of the dip is shown to be sudden or to occur over timescales too short to be compatible with even the highest estimates of M dwarf stellar winds, a trapped CME will be the likeliest cause of the dips. However, either way that the CME-stellar wind relationship plays out, determining the source of TIC 234284556’s accumulating plasma is an important next step. Considering that direct evidence for extra-solar CMEs is almost nonexistent (Alvarado-Gómez et al. 2019), a trapped CME cause might be especially interesting. However, if stellar winds are the source of the dip, that may allow us to better constrain  $\dot{M}_{wind}$  for young and magnetically active low-mass stars.

### 6.4. In the Context of Young Stars

TIC 234284556, being significantly brighter than any potential analogs, promises to become a benchmark system for understanding a whole class of stars with transiting magnetospheric clouds—systems potentially ranging from the 1.1 Myr B2 star  $\sigma$  Ori E to the 7-10 Myr binary M dwarf PTFO 8-8695 (Bouma et al. 2020b) to the 5-10 Myr transient flux-dip stars (Stauffer et al. 2017, 2018; Zhan et al. 2019; Stauffer et al. 2021).

It adds a new name to the short list of flux-dip stars that are candidates for centrifugal breakout, and at only  $\approx 44$  pc away compared to  $\approx 130$  pc for the other known centrifugal breakout candidates it is the best choice for follow-up observations. Moreover, at 45 million years old, TIC 234284556 is an older analog that will allow us to probe a new age-range, giving us a better un-

derstanding of how centrifugal breakout and magnetospheric clouds work at different evolutionary stages.

We take TIC 234284556 to be a good representative of these other systems, in part because they seem tied together by the following characteristics:

1. **Synchronously rotating dips** not well-explained by a typical transiting planet, but plausibly explained by magnetospheric clouds.
2. **Variable dips** with changing morphology, depth, and duration over relatively short timescales, and typically in a gradual manner.
3. **A Lack of an Infrared Excess**, in contrast with the class of dipper stars.
4. **Asymmetric and triangular dip profiles** in at least some cases.
5. **Youth, and strong rotational signals**, likely due at least in part to the fact that these are correlated with strong magnetic fields.
6. **H $\alpha$  emission**, with the shape consistent across all phases.
7. **One dominant dip** (though potentially with smaller secondary ones present), which distinguishes TIC 234284556 and its closest analogs—RIK-210 and the other transient flux-dip stars—from more distant relatives like  $\sigma$  Ori E and the persistent flux-dip stars introduced by [Stauffer et al. \(2017\)](#).
8. **Orbital period under 6 days**, a feature common to TIC 234284556, both transient and persistent flux-dip stars,  $\sigma$  Ori E, and PTFO 8-8695.
9. **Occasional sudden disappearances of dips**, sometimes accompanied by an unusually symmetric flare-like event, in a handful of the stars.

More work is needed to clarify which of these characteristics are essential to this emerging class of stars, and to establish where stars that share some, but not all, of these characteristics belong. For example,  $\sigma$  Ori E fits characteristics 1, 3, 5, 6, and 8; but there are two major dips and no noticeable variability in its dips characteristics over time ([Townsend et al. 2013](#)). Similarly, some of the persistent flux-dip stars have dips that disappear suddenly while accompanied by a flare-like event, but they, like  $\sigma$  Ori E, may have multiple mostly stable dips ([Stauffer et al. 2017](#)).

## 7. CONCLUSIONS AND FUTURE WORK

We have presented our analysis of TIC 234284556, a 45 Myr M dwarf, that has transit-like dips that change in depth and duration over two sectors of *TESS* data. Besides more gradual depth and duration variations that occur over  $\sim$ 10 day timescales, we take note of a sudden disappearance of the dip over a  $\sim$ 1 day period—and then see the dip reappear in LCO data about 100 days later. We have shown that this behavior can be explained by a magnetospheric cloud and centrifugal breakout scenario and have found the data to be inconsistent with our other explanations.

When considered alongside the handful of centrifugal breakout candidates among the known flux-dip stars, we argue that we now have observational evidence that centrifugal breakout plays a role in mass-loss processes for at least some classes of stars—this despite the fact that previous non-detections of centrifugal breakout led astronomers to consider alternative mass-loss mechanisms. Moreover, TIC 234284556 hints at the possibility of uniting a class of mysterious young stars ranging from  $\sigma$  Ori E and PTFO 8-8695 to the known flux-dip stars.

However TIC 234284556 stands out among its potential analogs. It is older, allowing us a glimpse into a different evolutionary stage for this class of stars. It has a long baseline, with more than two years of data, which allows for a better understanding of the transiting dips. This baseline provides the opportunity to observe what appears to be three different dip origins and one phase change. And, most importantly, TIC 234284556 is the brightest of its class of low-mass stars, making it the best choice for follow-up studies and potentially the archetypal system of this kind.

In particular, future X-ray observations of TIC 234284556, planned for 2021 with XMM-Newton, may shed light on the origin and structure of these dips. Simultaneous multi-color time-series photometry, ideally via a southern analog of MuSCAT or MuSCAT2 ([Narita et al. 2015, 2019](#)) given TIC 234284556's declination  $\delta$  of  $-63^\circ$ , could give a definitive confirmation of the dips' chromaticity. Future magnetic field measurements, potentially via Zeeman broadening (e.g. [Kochukhov 2021](#)), could allow us to test the [Townsend & Owocki \(2005\)](#) rigidly rotating magnetosphere model empirically. And tighter photometric constraints on the timescales involved in the reappearance of the dips could allow us to distinguish between the two mass-accumulation mechanisms, CMEs and stellar winds, while potentially adding to currently scanty evidence of extrasolar CMEs or allowing us to more tightly constrain M dwarf stellar wind rates, which, at the moment, are uncertain to five orders of magnitude ([Vidotto et al. 2013](#)).

## ACKNOWLEDGMENTS

We thank Richard Townsend, Katja Poppenhaeger, Trevor David, and Christina Hedges for thought-provoking conversations and insights into the TIC 234284556 system which improved the quality of this manuscript. We thank Chris Tinney for helpful discussions on Veloce observing modes. E.K.P. thanks Nils Palumbo (University of Wisconsin-Madison) for much-appreciated coding advice, the NEarby Worlds and Their Stars (NEWTS) group (PI: Benjamin Montet, UNSW) for welcoming her into their lab group, and the Caltech Beans for moral support throughout the research process.

This paper relies on data from the *TESS* mission, which is funded by the NASA Explorer Program. *TESS* data were obtained from the Mikulski Archive for Space Telescopes (MAST), which is supported in part by the NASA Office of Space Science's grant NNX13AC07G.

This research made use of the SIMBAD database, operated at CDS, Strasbourg, France and of the Exoplanet Follow-up Observation Program (ExoFOP) website, which is operated by the Caltech, under contract with NASA via the Exoplanet Exploration Program.

This work used data from the European Space Agency (ESA) mission *Gaia* (<https://www.cosmos.esa.int/gaia>), processed by the *Gaia* Data Processing and Analysis Consortium (DPAC, <https://www.cosmos.esa.int/web/gaia/dpac/consortium>). Funding for the DPAC has been provided by national institutions, in particular the institutions participating in the *Gaia* Multilateral Agreement.

This work makes use of observations from the Las Cumbres Observatory global telescope network, in particular the Sinistro camera on the LCOGT-1m telescope at the South African Astronomical Observatory. The LCOGT observations were conducted under the auspices of NOIRLab program NOAO2020B-013 (PI: J. Hartman).

This research also made use of ASAS-SN data. ASAS-SN is funded by the Gordon and Betty Moore Foundation under the 5 year grant GBMF5490 as well as by the National Science Foundation under grants AST-151592 and AST-1908570, with telescopes hosted by LCO.

This work was also based in part on data obtained at the Anglo-Australian Telescope under program A/2020B/09. We acknowledge the traditional owners of the land on which the AAT stands, the Gamilaraay people, and pay our respects to elders past and present.

This material is based upon work supported by the National Science Foundation Graduate Research Fellowship Program under Grant No. DGE-1746045.

E.K.P.'s role in this research was funded by Caltech's Summer Undergraduate Research Fellowship (SURF) program, with generous support from Harold and Mary Zirin.

L.G.B. and J.H. acknowledge support by the TESS GI Program, programs G011103 and G022117, through NASA grants 80NSSC19K0386 and 80NSSC19K1728. J.H. acknowledges additional support from NASA grant NNX17AB61G.

*Facilities:* *TESS* ASAS-SN, LCOGT (SAAO), Siding Spring Observatory (Veloce), MAST, Simbad

*Software:* numpy (Van Der Walt et al. 2011), matplotlib (Hunter et al. 2007), lightkurve (Lightkurve Collaboration et al. 2018), exoplanet (Foreman-Mackey et al. 2020; Salvatier et al. 2016a; Theano Development Team 2016), pymc3 (Salvatier et al. 2016b), transitleast-squares (Hipke & Heller 2019), statsmodels (Seabold & Perktold 2010), itertools (Van Rossum 2020), scipy (Jones et al. 2001), astropy (Price-Whelan et al. 2018), eleanor (Feinstein et al. 2019), stella (Feinstein et al. 2020a), emcee (Foreman-Mackey et al. 2013), pickle (Van Rossum 2020), os, uncertainties (Lebigot 2010), peakdet (Billauer 2011), Mathematica (Wolfram Research 2020), CurveFit (Caltech 2021)

## REFERENCES

Alvarado-Gómez, J. D., Drake, J. J., Cohen, O., Moschou, S. P., & Garraffo, C. 2018, The Astrophysical Journal, 862, 93. <http://dx.doi.org/10.3847/1538-4357/aacb7f>

Alvarado-Gómez, J. D., Drake, J. J., Garraffo, C., et al. 2019, Proceedings of the International Astronomical Union, 15, 407–413. <http://dx.doi.org/10.1017/S1743921320001465>

Ansdel, M., Gaidos, E., Rappaport, S. A., et al. 2016, The Astrophysical Journal, 816, 69. <http://dx.doi.org/10.3847/0004-637X/816/2/69>

Ansdel, M., Gaidos, E., Hedges, C., et al. 2019, Monthly Notices of the Royal Astronomical Society, 492, 572–588. <http://dx.doi.org/10.1093/mnras/stz3361>

Bailer-Jones, C. A. L., Rybizki, J., Fouesneau, M., Demleitner, M., & Andrae, R. 2021, VizieR Online Data Catalog, I/352

Barnes, J. W., van Eyken, J. C., Jackson, B. K., Ciardi, D. R., & Fortney, J. J. 2013, The Astrophysical Journal, 774, 53. <http://dx.doi.org/10.1088/0004-637X/774/1/53>

Bell, C., Mamajek, E., & Naylor, T. 2015, Monthly Notices of the Royal Astronomical Society, 454, doi:10.1093/mnras/stv1981

Belokurov, V., Penoyre, Z., Oh, S., et al. 2020, Monthly Notices of the Royal Astronomical Society, 496, 1922–1940. <http://dx.doi.org/10.1093/mnras/staa1522>

Benz, A. O., & Güdel, M. 2010, ARA&A, 48, 241

Billauer, E. 2011, . . . <https://gist.github.com/endolith/250860>

Bodman, E. H. L., Quillen, A. C., Ansdell, M., et al. 2017, MNRAS, 470, 202

Bouma, L. G., Winn, J. N., Ricker, G. R., et al. 2020a, AJ, 160, 86

Bouma, L. G., Hartman, J. D., Brahm, R., et al. 2020b, AJ, 160, 239

Boyajian, T. S., LaCourse, D. M., Rappaport, S. A., et al. 2016, Monthly Notices of the Royal Astronomical Society, 457, 3988–4004. <http://dx.doi.org/10.1093/mnras/stw218>

Brown, T. M., Baliber, N., Bianco, F. B., et al. 2013, PASP, 125, 1031. <http://adsabs.harvard.edu/abs/2013PASP..125.1031B>

Caltech, S. P. L. 2021, . . . [http://www.sophphx.caltech.edu/Physics\\_6/CurveFit/](http://www.sophphx.caltech.edu/Physics_6/CurveFit/)

Cody, A. M., & Hillenbrand, L. A. 2010, ApJS, 191, 389

—. 2018, AJ, 156, 71

Cranmer, S. R. 2017, The Astrophysical Journal, 840, 114. <http://dx.doi.org/10.3847/1538-4357/aa6f0e>

Crundall, T. D., Ireland, M. J., Krumholz, M. R., et al. 2019, MNRAS, 489, 3625

Cutri, R. M., Skrutskie, M. F., van Dyk, S., et al. 2003, VizieR Online Data Catalog, II/246

Cutri, R. M., Wright, E. L., Conrow, T., et al. 2021, VizieR Online Data Catalog, II/328

David, T. J., Hillenbrand, L. A., Petigura, E. A., et al. 2016, Nature, 534, 658–661. <http://dx.doi.org/10.1038/nature18293>

David, T. J., Petigura, E. A., Hillenbrand, L. A., et al. 2017, The Astrophysical Journal, 835, 168. <http://dx.doi.org/10.3847/1538-4357/835/2/168>

Denis, C. 2005, VizieR Online Data Catalog, B/denis

Faigler, S., Tal-Or, L., Mazeh, T., Latham, D. W., & Buchhave, L. A. 2013, The Astrophysical Journal, 771, 26. <http://dx.doi.org/10.1088/0004-637X/771/1/26>

Feigelson, E. D., Giampapa, M. S., & Vrba, F. J. 1991, in The Sun in Time, ed. C. P. Sonett, M. S. Giampapa, & M. S. Matthews, 658

Feinstein, A., Montet, B., & Ansdell, M. 2020a, The Journal of Open Source Software, 5, 2347

Feinstein, A. D., Montet, B. T., Ansdell, M., et al. 2020b, AJ, 160, 219

Feinstein, A. D., Montet, B. T., Foreman-Mackey, D., et al. 2019, Publications of the Astronomical Society of the Pacific, 131, 094502. <http://dx.doi.org/10.1088/1538-3873/ab291c>

Foreman-Mackey, D., Agol, E., Ambikasaran, S., & Angus, R. 2017, The Astronomical Journal, 154, 220. <http://dx.doi.org/10.3847/1538-3881/aa9332>

Foreman-Mackey, D., Hogg, D. W., Lang, D., & Goodman, J. 2013, PASP, 125, 306

Foreman-Mackey, D., Luger, R., Czekala, I., et al. 2020, exoplanet-dev/exoplanet v0.3.2, . . . doi:10.5281/zenodo.1998447. <https://doi.org/10.5281/zenodo.1998447>

Gagné, J., Mamajek, E. E., Malo, L., et al. 2018, ApJ, 856, 23

Gaia Collaboration. 2018, VizieR Online Data Catalog, I/345

—. 2020, VizieR Online Data Catalog, I/350

Gaia Collaboration, Brown, A. G. A., Vallenari, A., et al. 2020, arXiv e-prints, 2012, arXiv:2012.01533. <http://adsabs.harvard.edu/abs/2020arXiv201201533G>

Getman, K. V., & Feigelson, E. D. 2021, arXiv:2105.04768

Gilbert, J., Bergmann, C., Bloxham, G., et al. 2018, in Society of Photo-Optical Instrumentation Engineers (SPIE) Conference Series, Vol. 10702, Ground-based and Airborne Instrumentation for Astronomy VII, ed. C. J. Evans, L. Simard, & H. Takami, 107020Y

Gregory, S. G., Donati, J. F., Morin, J., et al. 2012, ApJ, 755, 97

Groote, D., & Hunger, K. 1977, A&A, 56, 129

Günther, M. N., Zhan, Z., Seager, S., et al. 2020, AJ, 159, 60

Günther, M. N., Berardo, D. A., Ducrot, E., et al. 2020, arXiv:2008.11681 [astro-ph], arXiv: 2008.11681. <http://arxiv.org/abs/2008.11681>

Hamann, A., Montet, B. T., Fabrycky, D. C., Agol, E., & Kruse, E. 2019, The Astronomical Journal, 158, 133. <http://dx.doi.org/10.3847/1538-3881/ab32e3>

Hauschildt, P. H., Allard, F., & Baron, E. 1999, ApJ, 512, 377

Hedges, C., Hodgkin, S., & Kennedy, G. 2018, Monthly Notices of the Royal Astronomical Society, 476, 2968–2998. <http://dx.doi.org/10.1093/mnras/sty328>

Hernández, J., Calvet, N., Perez, A., et al. 2014, ApJ, 794, 36

Hipke, M., & Heller, R. 2019, A&A, 623, A39

Honda, S., Notsu, Y., Namekata, K., et al. 2018, PASJ, 70, 62

Howard, W. S., Corbett, H., Law, N. M., et al. 2020, The Astrophysical Journal, 902, 115.  
<http://dx.doi.org/10.3847/1538-4357/abb5b4>

Hunt-Walker, N. M., Hilton, E. J., Kowalski, A. F., Hawley, S. L., & Matthews, J. M. 2012, Publications of the Astronomical Society of the Pacific, 124, 545–551.  
<http://dx.doi.org/10.1086/666495>

Hunter, J. D., et al. 2007, Computing in science and engineering, 9, 90

Jardine, M., Cameron, A. C., Donati, J.-F., & Hussain, G. A. J. 2019, Monthly Notices of the Royal Astronomical Society, doi:10.1093/mnras/stz3173.  
<http://dx.doi.org/10.1093/mnras/stz3173>

Jardine, M., & Collier Cameron, A. 2018, Monthly Notices of the Royal Astronomical Society, 482, 2853–2860.  
<http://dx.doi.org/10.1093/mnras/sty2872>

Jayasinghe, T., Kochanek, C. S., Stanek, K. Z., et al. 2021, MNRAS, 503, 200

Jenkins, J. M., Twicken, J. D., McCauliff, S., et al. 2016, in Society of Photo-Optical Instrumentation Engineers (SPIE) Conference Series, Vol. 9913, Software and Cyberinfrastructure for Astronomy IV, ed. G. Chiozzi & J. C. Guzman, 99133E

Johnstone, C. P., Jardine, M., Gregory, S. G., Donati, J.-F., & Hussain, G. 2013, Monthly Notices of the Royal Astronomical Society, 437, 3202–3220.  
<http://dx.doi.org/10.1093/mnras/stt2107>

Jones, E., Oliphant, T., Peterson, P., & et al. 2001.  
<http://www.scipy.org/>

Kobayashi, H., Kimura, H., Watanabe, S. i., Yamamoto, T., & Müller, S. 2011, Earth, Planets, and Space, 63, 1067

Kochukhov, O. 2021, A&A Rv, 29, 1

Kraus, A. L., Shkolnik, E. L., Allers, K. N., & Liu, M. C. 2014, The Astronomical Journal, 147, 146.  
<http://dx.doi.org/10.1088/0004-6256/147/6/146>

Lebigot, E. 2010, . . . <https://uncertainties-python-package.readthedocs.io/en/latest/>

Lieshout, R. v., & Rappaport, S. A. 2018, Handbook of Exoplanets, 1527–1544.  
[http://dx.doi.org/10.1007/978-3-319-55333-7\\_15](http://dx.doi.org/10.1007/978-3-319-55333-7_15)

Lightkurve Collaboration, Cardoso, J. V. d. M., Hedges, C., et al. 2018, Lightkurve: Kepler and TESS time series analysis in Python, Astrophysics Source Code Library, , , ascl:1812.013

Maehara, H., Notsu, Y., Namekata, K., et al. 2021, PASJ, 73, 44

Mandel, K., & Agol, E. 2002, ApJL, 580, L171

Mann, A. W., Johnson, M. C., Vanderburg, A., et al. 2020, AJ, 160, 179

Mazeh, T., & Faigler, S. 2010, A&A, 521, L59

McGinnis, P. T., Alencar, S. H. P., Guimarães, M. M., et al. 2015, A&A, 577, A11

McLaughlin, D. B. 1924, ApJ, 60, 22

Narita, N., Fukui, A., Kusakabe, N., et al. 2015, Journal of Astronomical Telescopes, Instruments, and Systems, 1, 045001, arXiv: 1509.03154.  
<http://arxiv.org/abs/1509.03154>

—. 2019, Journal of Astronomical Telescopes, Instruments, and Systems, 5, 015001.  
<http://adsabs.harvard.edu/abs/2019JATIS...5a5001N>

Oksala, M. E., Wade, G. A., Townsend, R. H. D., Kochukhov, O., & Owocki, S. P. 2010, Proceedings of the International Astronomical Union, 6, 124–129

Oksala, M. E., Kochukhov, O., Krčka, J., et al. 2015, MNRAS, 451, 2015

Onitsuka, M., Fukui, A., Narita, N., et al. 2017, PASJ, 69, doi:10.1093/pasj/psx004.  
<https://academic.oup.com/pasj/article/69/2/L2/2996563>

Osten, R., Livio, M., Lubow, S., et al. 2013, The Astrophysical Journal, 765, L44.  
<http://dx.doi.org/10.1088/2041-8205/765/2/L44>

Osten, R. A., & Wolk, S. J. 2015, The Astrophysical Journal, 809, 79.  
<http://dx.doi.org/10.1088/0004-637X/809/1/79>

Owocki, S. P., & Cranmer, S. R. 2017, Monthly Notices of the Royal Astronomical Society, 474, 3090–3100.  
<http://dx.doi.org/10.1093/mnras/stx2989>

Owocki, S. P., Shultz, M. E., ud Doula, A., et al. 2020, Monthly Notices of the Royal Astronomical Society, 499, 5366–5378. <http://dx.doi.org/10.1093/mnras/staa2325>

Pál, A. 2012, MNRAS, 421, 1825

Price-Whelan, A. M., Sipőcz, B. M., Günther, H. M., et al. 2018, AJ, 156, 123

Rappaport, S., Levine, A., Chiang, E., et al. 2012, The Astrophysical Journal, 752, 1.  
<http://dx.doi.org/10.1088/0004-637X/752/1/1>

Reinhold, T., & Gizon, L. 2015, A&A, 583, A65

Ricker, G. R., Winn, J. N., Vanderspek, R., et al. 2014, in Proc. SPIE, Vol. 9143, Space Telescopes and Instrumentation 2014: Optical, Infrared, and Millimeter Wave, 914320

Ricker, G. R., Winn, J. N., Vanderspek, R., et al. 2014, Journal of Astronomical Telescopes, Instruments, and Systems, 1, 014003.  
<http://dx.doi.org/10.1117/1.JATIS.1.1.014003>

Rizzuto, A. C., Newton, E. R., Mann, A. W., et al. 2020, *The Astronomical Journal*, 160, 33. <http://dx.doi.org/10.3847/1538-3881/ab94b7>

Rossiter, R. A. 1924, *ApJ*, 60, 15

Salvatier, J., Wiecki, T. V., & Fonnesbeck, C. 2016a, *PeerJ Computer Science*, 2, e55

—. 2016b, *PeerJ Computer Science*, 2, e55. <https://doi.org/10.7717/peerj-cs.55>

Sanchis-Ojeda, R., Rappaport, S., Pallè, E., et al. 2015, *The Astrophysical Journal*, 812, 112. <http://dx.doi.org/10.1088/0004-637X/812/2/112>

Scholz, A., Coffey, J., Brandeker, A., & Jayawardhana, R. 2007, *ApJ*, 662, 1254

Seabold, S., & Perktold, J. 2010, in 9th Python in Science Conference

Shappee, B. J., Prieto, J. L., Grupe, D., et al. 2014, *ApJ*, 788, 48

Shultz, M. E., Owocki, S., Rivinius, T., et al. 2020, *Monthly Notices of the Royal Astronomical Society*, 499, 5379–5395. <http://dx.doi.org/10.1093/mnras/staa3102>

Shulyak, D., Reiners, A., Nagel, E., et al. 2019, *A&A*, 626, A86

Stassun, K. G., Oelkers, R. J., Pepper, J., et al. 2018, *AJ*, 156, 102

Stassun, K. G., Oelkers, R. J., Paegert, M., et al. 2019, *The Astronomical Journal*, 158, 138. <http://dx.doi.org/10.3847/1538-3881/ab3467>

Stauffer, J., Cody, A. M., McGinnis, P., et al. 2015, *AJ*, 149, 130

Stauffer, J., Cameron, A. C., Jardine, M., et al. 2017, *The Astronomical Journal*, 153, 152. <http://dx.doi.org/10.3847/1538-3881/aa5eb9>

Stauffer, J., Rebull, L., David, T. J., et al. 2018, *The Astronomical Journal*, 155, 63. <http://dx.doi.org/10.3847/1538-3881/aaa19d>

Stauffer, J., Rebull, L. M., Jardine, M., et al. 2021, *The Astronomical Journal*, 161, 60. <http://dx.doi.org/10.3847/1538-3881/abc7c6>

Tanimoto, Y., Yamashita, T., Ui, T., et al. 2020, *Publications of the Astronomical Society of Japan*, 72, doi:10.1093/pasj/psz145. <http://dx.doi.org/10.1093/pasj/psz145>

Tanimoto, Y., Yamashita, T., Ui, T., et al. 2020, *PASJ*, arXiv:2001.00148

Theano Development Team. 2016, arXiv e-prints, abs/1605.02688. <http://arxiv.org/abs/1605.02688>

Tielens, A. G. G. M. 2005, *The Physics and Chemistry of the Interstellar Medium* (Cambridge University Press), doi:10.1017/CBO9780511819056

Townsend, R. H. D. 2007, in *Astronomical Society of the Pacific Conference Series*, Vol. 361, *Active OB-Stars: Laboratories for Stellare and Circumstellar Physics*, ed. A. T. Okazaki, S. P. Owocki, & S. Stefl, 110

Townsend, R. H. D., & Owocki, S. P. 2005, *Monthly Notices of the Royal Astronomical Society*, 357, 251. <https://onlinelibrary.wiley.com/doi/abs/10.1111/j.1365-2966.2005.08642.x>

Townsend, R. H. D., Rivinius, T., Rowe, J. F., et al. 2013, *ApJ*, 769, 33

ud-Doula, A., Townsend, R. H. D., & Owocki, S. P. 2006, *ApJL*, 640, L191

Van Der Walt, S., Colbert, S. C., & Varoquaux, G. 2011, *Computing in Science & Engineering*, 13, 22

van Eyken, J. C., Ciardi, D. R., von Braun, K., et al. 2012, *The Astrophysical Journal*, 755, 42. <http://dx.doi.org/10.1088/0004-637X/755/1/42>

Van Rossum, G. 2020, *The Python Library Reference*, release 3.8.2 (Python Software Foundation)

Vanderburg, A., Johnson, J. A., Rappaport, S., et al. 2015, *Nature*, 526, 546–549. <http://dx.doi.org/10.1038/nature15527>

Vidotto, A. A., Jardine, M., Morin, J., et al. 2013, *Monthly Notices of the Royal Astronomical Society*, 438, 1162–1175. <http://dx.doi.org/10.1093/mnras/stt2265>

Vidotto, A. A., Gregory, S. G., Jardine, M., et al. 2014, *Monthly Notices of the Royal Astronomical Society*, 441, 2361–2374. <http://dx.doi.org/10.1093/mnras/stu728>

Waggoner, A. R., & Cleeves, L. I. 2019, *ApJ*, 883, 197

Waugh, R. F. P., Jardine, M. M., Morin, J., & Donati, J.-F. 2021, arXiv:2106.05772

Williams, J. P., & Cieza, L. A. 2011, *ARA&A*, 49, 67

Wolfram Research, I. 2020, *Mathematica*, Version 12.2, , , champaign, IL, 2020. <https://www.wolfram.com/mathematica>

Yu, L., Winn, J. N., Gillon, M., et al. 2015, *The Astrophysical Journal*, 812, 48. <http://dx.doi.org/10.1088/0004-637X/812/1/48>

Zacharias, N., Finch, C. T., Girard, T. M., et al. 2012, *VizieR Online Data Catalog*, I/322A

Zaire, B., Donati, J.-F., & Klein, B. 2021, arXiv e-prints, arXiv:2104.02619

Zhan, Z., Günther, M. N., Rappaport, S., et al. 2019, *ApJ*, 876, 127